FEASIBILITY OF GROUND-PENETRATING RADAR FOR USE AT MGP SITES

FINAL REPORT

R. G. Plumb, P. Chaturvedi,
K. R. Demarest, Z. Huang,
S. Chakrabarti, and S. Ng

Radar Systems and Remote Sensing Laboratory
Department of Electrical Engineering and Computer Science, University of Kansas
2291 Irving Hill Road, Lawrence, Kansas 66045-2969
TEL: 913/864-4835 * FAX: 913/864-7789 * OMNET: KANSAS.U.RSL

RSL Technical Report 9990-5

June 1994

Sponsored by:

Electric Power Research Institute
P. O. Box 10412, Palo Alto CA 94303

Agreement RP2879-27

FEASIBILITY OF GROUND-PENETRATING RADAR FOR USE AT MGP SITES

FINAL REPORT

R. G. Plumb, P. Chaturvedi,
K. R. Demarest, Z. Huang,
S. Chakrabarti, and S. Ng

Radar Systems and Remote Sensing Laboratory
Department of Electrical Engineering and Computer Science, University of Kansas
2291 Irving Hill Road, Lawrence, Kansas 66045-2969
TEL: 913/864-4835 * FAX: 913/864-7789 * OMNET: KANSAS.U.RSL

RSL Technical Report 9990-5

June 1994

Sponsored by:

Electric Power Research Institute
P. O. Box 10412, Palo Alto CA 94303

Agreement RP2879-27

Feasibility of Ground-Penetrating Radar for Use at MGP Sites

Final Report, June 1994

Prepared by

THE UNIVERSITY OF KANSAS
Radar Systems and Remote Sensing Laboratory
Department of Electrical Engineering and Computer Science
Lawrence, Kansas 66045

Principal Investigators

Richard G. Plumb
Pawan Chaturvedi
Kenneth R. Demarest
Zhubo Huang
Swapan Chakrabrati
Sei Ng

Prepared for

Electric Power Research Institute
3412 Hillview Avenue
Palo Alto, CA 94304

Dr. Ishawr Murarka, EPRI Project Manager

and

Kansas Electric Utilities Research Program
700 SW Harrison, Suite 1430
Topeka, KS 66601

Jerry Lonergan, KEURP Executive Director

DISCLAIMER OF WARRANTIES AND LIMITATION OF LIABILITIES

Executive Summary

In this investigation, we examined the issues associated with using ground-penetrating radars for detecting and imaging subsurface contaminates. By developing advanced electromagnetic signal processing techniques, we have shown through computer simulations that ground-penetrating radars are capable of detecting and imaging low contrast contaminates, characteristics associated with hydrocarbon contaminates.

A ground-penetrating radar, or GPR, is an electrical device that detects buried objects (targets) by transmitting and receiving electromagnetic energy. The detection process begins by generating an impulsive signal, typically on the order of 50 nanoseconds. This short-time signal is radiated by the transmit antenna forming the incident electromagnetic field in the ground. A portion of the incident field is reflected, or scattered, off any buried target and the radar records this scattered field. By comparing the incident field to the measured scattered field, a GPR is capable of obtaining information about a particular target.

The strength of the signal received by the GPR depends on several factors such as the contrast between the background soil and the object, the depth of the object, and the amount of ohmic loss in the soil. Generally, the larger the electrical contrast between the object and the background medium, the larger the scattered signal. The deeper the object is, the smaller the received signal becomes. This is due mainly to attenuation of the electromagnetic fields as they propagate through the soil. The amount of attenuation, or ohmic losses, depends on soil type and the operating frequency of the radar. Overall, attenuation increases with frequency and the amount of water in the soil.

A traditional GPR employs separate transmit and receive antennas, which are usually collocated in a so-called monostatic configuration. The GPR generates and transmits pulses at a set periodic rate on the order of 100 pulses per second. The received signals are recorded and displayed. A GPR determines the distance to a target, and thereby detects a target by measuring the time it takes the transmitted signal to travel from the radar to the target and back again. Most GPR systems do not perform any type of signal processing on the received signals. If a buried object is located at a particular depth below the ground, the received signal will be relatively large at the corresponding time-range.

Typical hydrocarbon contaminates form low contrast plumes (objects) with most background soils. A convention monostatic GPR employing no signal processing will have

difficulty in detecting and mapping such objects. However, if a bistatic configuration in which the transmit and receive antennas are moved around separately, and advanced signal processing is used, hydrocarbon contaminates can be detected and imaged.

In this investigation we developed advanced signal processing techniques capable of imaging low contrast targets. These techniques are based upon formulating the subsurface imaging problem as an inverse electromagnetic scattering problem. We solve the inverse scattering problem using either the Born iterative technique or diffraction tomography. To properly image a buried target requires that data be taken at many transmit/receive locations. For each separate location of the transmit antenna, data must be recorded at several locations around the transmit antenna. Further information on the target, and therefore better images, are obtained if the receive antenna is place in a vertical borehole near the object in conjunction with surface locations.

To test the theories developed in this investigation, we programmed a ground-penetrating radar simulator using full-wave electromagnetic techniques. Our GPR simulator is based upon the finite-difference time-domain algorithm which is a direct numerical implementation of Maxwell's electromagnetic equations. Our simulator properly accounts for the air-to-soil interface and can model heterogeneous soils and targets.

We tested the Born iterative and diffraction tomography imaging algorithms using data generated by our GPR simulator. Our simulations show that low contrast objects can be imaged where traditional monostatic GPRs failed. The imaging algorithms we developed provide information on the object's shape as well as an estimate of its electrical properties. Estimates of the object's electrical properties can be used in classifying the object. We began a preliminary investigation in classifying subsurface images using artificial neural networks. Although strictly preliminary at this time, it does appear that neural networks are useful in classifying certain types of buried objects.

If developed to their full potential, the theories and techniques presented in this report could be used in generating accurate subsurface images of suspected spill sites. These images or underground maps would be a valuable tool in determining the extent of a site cleanup.

Acknowledgment

The authors gratefully acknowledge Mr. Kenneth J. Ladwig, Vice President, Science & Technology Management, Inc., for his support, guidance, and management throughout this project. We also wish to express our thanks to Mr. Wade Graves, Manager, Electric Research & Development, Kansas Public Lighting, for suggesting this research topic.

Contents

List of Illustrations

List of Tables

I. INTRODUCTION

A problem facing utility companies today is identifying and locating spill sites and buried objects. Underground objects include gas and electric lines, discarded transformers and oil tanks. Over time, some of these objects may start to leak their contents. When PCBs and oil leak, for example, a site assessment is called for. If the site is contaminated, a general cleanup of the site may be required. Currently, soil core samples are needed to determine if a spill has occurred. Once a potential site has been identified, many samples are required to adequately test for spills. Even then, there is no guarantee that part of the site has not been missed. Therefore, a better method of site assessment of suspected spill zones is needed. This report will discuss the use of ground-penetrating radars to detect, image, and classify subsurface contamination.

Ground-penetrating radar (GPR) techniques have been used for over 20 years to detect and locate subsurface objects. The areas of application are diverse and include geological prospecting, civil engineering site investigations, highway investigations, polar ice sheet investigations, as well as the detection and location of buried pipes, cables, and barrels. Recent advances in RF and digital electronics, polarimetric signal processing, as well as the computational power of microprocessors, make GPR a prime candidate for the detection and mapping of subsurface contaminates.

GPR offers the potential for rapid, non-invasive mapping of subsurface features. A radar is an extremely sensitive electronic device that generates, transmits, and receives electromagnetic waves. The operation of a radar is straightforward. An electromagnetic wave is generated by the radar and transmitted into the ground. When the incident wave strikes any discontinuity, a scattered wave is reflected back to the radar and the radar records this signal. By comparing the incident and scattered waves, it is possible to infer information about the object that scattered the wave. These objects may be discrete, such as pipes and barrels, or distributed, such as a chemical plume or coal tar.

The purpose of this report is to show that ground-penetrating radars are useful in detecting subsurface contaminates such as coal tar located at manufactured gas plant sites. This reports concentrates on a numerical simulation of two-dimensional GPR data. Subsurface maps, or images, are generated and classified from the simulated data. Images are generated by solving an inverse electromagnetic scattering problem using

either diffraction tomography or a Born iterative method. The images generated from the radar data are then classified using artificial neural networks.

This study presents a detailed analysis on four major aspects of detecting subsurface contaminates using ground-penetrating radars: (1) modeling the background soil and subsurface contaminates; (2) developing an electromagnetic GPR simulator using the finite-difference time-domain technique; (3) generating subsurface maps using specialized inverse electromagnetic scattering techniques; and (4) classifying images using neural networks.

II. BACKGROUND INFORMATION

A scattered wave is generated whenever an incident electromagnetic wave encounters a change in an electrical constitutive parameter in the soil. There are three constitutive parameters that characterize all material. They are permittivity, permeability, and conductivity. Most soils are non-magnetic and, therefore, no change in the permeability is expected. At low frequencies, below roughly 20 MHz, the conductivity is the dominant constitutive parameter, while the permittivity is the dominant parameter for operations above 20 MHz. When the conductivity is the dominant constitutive parameter, the electric and magnetic fields diffuse through the soil. On the other hand, when the permittivity is the dominant parameter, the electric and magnetic fields propagate through the soil. Wave propagation and diffusion are two different phenomena, and different systems are used to explot their individual characteristics. In this investigation we rely on wave propagation in the soil.

Most GPR systems rely on wave propagation and, therefore, operate in the 100- to 1,500 MHz range. Electromagnetic sounding systems, on the other hand, are designed to operate when diffusion is the dominant mode of advancing the electric and magnetic fields. Both systems have advantages and disadvantages, which are mainly linked to the issues of depth of penetration and resolution. Both systems rely on measuring a scattered signal of sufficient strength. These issues are explained below.

The strength of the scattered wave received by the electromagnetic system depends, in part, on the contrast in constitutive parameters between the background soil and the scattering object: the greater the contrast the larger the scattered wave. In addition, the shape of the object also contributes to the strength of the scattered wave. A large flat plate will scatter electromagnetic energy differently than a long thin pipe. By knowing the characteristics of the desired class of targets, for example long, and thin for pipes, it is possible to tailor the radar design to preferentially detect that class of target over all other objects.

Many factors influence the design of any probing radar. The principal constraint on the design process is the set of electromagnetic properties (permittivity, permeability, and conductivity) of the medium under test. These parameters, in conjunction with the required depth of penetration and resolution requirements, place limits on the operating frequency of the radar. Resolution is the ability of the radar to distinguish between two closely spaced targets. A radar has two types of resolution, range resolution and horizontal resolution, which

are orthogonal to each other. Range resolution is proportional to the inverse of the received signal bandwidth, which is the difference between the highest and lowest frequencies of the received signal. Therefore fine range resolution requires a transmitted waveform having a large bandwidth. The horizontal, or cross-range, resolution of the radar is determined by the antenna beamwidth: the narrower the beamwidth the finer the horizontal resolution. Cross-range resolution can be increased by using synthetic aperture processing.

There are trade-offs associated with transmitting broadband waveforms. All soils attenuate electromagnetic energy, and the attenuation usually increases with increasing frequency and moisture content. If large penetration depths are required, the transmitted waveform should be low in frequency. However, large signal bandwidths are impossible to obtain when transmitting low frequencies. Therefore a trade-off between range resolution and depth of penetration must be made. Since GPR systems operate at higher frequencies, GPR provide better resolution than electromagnetic sounding systems. However, sounding systems can detect objects much deeper than GPR.

Frequency-modulated continuous-wave (FM-CW) radars and impulse radars are two types of radars used in GPR applications requiring broadband waveforms. Since both radars are broadband, they have good range resolution, but the methods by which they obtain the broadband signals differ. The impulse radar can be thought of as a time-domain approach, while the FM-CW radar uses a frequency-domain approach. An impulse radar generates and transmits a very narrow time pulse. A narrow time pulse has a very broad signal spectrum leading to a broadband waveform. The major problem associated with the impulse radar is the antenna design; antennas tend to be narrowband devices. When a narrow time signal is transmitted through a narrowband antenna the antenna rings or oscillates. Ringing is a problem because it can mask targets. To overcome ringing, the antennas on impulse radars must be loaded, reducing the overall efficiency. In addition to low efficiency antennas, impulse radars have low duty cycles and thus require higher amounts of peak power.

An FM-CW radar obtains its broad bandwidth by directly generating a signal that has a broad spectrum. This is accomplished by continuously sweeping the transmitted frequency from some low value, f_{low} , to a high value, f_{high}, at a typical sweep rate of 100 Hz. The resulting bandwidth is then f_{high}-f_{low}. Since the FM-CW radar is continuously transmitting, it has a duty cycle of 100% thus requiring lower peak power than impulse radars.

The advantages the FM-CW radar have are antenna design, transmitted spectral shape, and a better suitability for certain types of signal processing. Since the radar transmits a continuous wave, the antenna design for an FM-CW radar is simpler than that for the impulse radar. The FM-CW radar also provides easier control over the transmitted spectral shape of the waveform. The transmitted waveform is continuously swept in frequency between preset limits. Any fluctuations in antenna gain can easily be compensated, allowing for any desired spectral shape. Control of spectral shape is important in many signal processing techniques used to extract target information. The received signal is then mixed with a portion of the currently transmitted signal giving a difference frequency, which depends on the target depth. This type of signal recovery preserves both the amplitude and phase of the backscattered signal.

A variant of the FM-CW GPR is the stepped-FM radar. Instead of continuously sweeping the frequency between preset limits, as in FM-CW radars, the frequencies generated by a stepped-FM radar are discrete. The frequency band is divided into N segments, where N is usually a power of 2, and the radar steps through the frequencies. The advantage of stepped-FM radars is the repeatability and stability offered by inexpensive, synthesized sources that are commercially available. Synthesized sources are usually phase-locked thus allowing for coherent processing.

The three types of GPRs just described-impulse, FM-CW, and stepped FM-usually have separate transmit and recieve antennas. In most applications, the two antennas are located in close proximity to each other and the radar is refered to as a monostatic radar. More information about the target may be obtained if the transmit and receive antennas are moved separately about the object. When the antennas are displaced from each other, the radar is said to be in a bistatic mode.

Since one of the goals of this project was to image subsurface contaminates, a bistatic mode of operation was selected. The bistatic mode of operation lends itself to better images. In the following section the details of the analysis of the project are presented.

III. ANALYSIS

A. TARGET MODELING AND SOIL CHARACTERIZATION

Realistic models of soil and contaminants are necessary for testing the capability of any GPR system. Soil and contaminant properties have been investigated in detail in the past and the reader is referred to [1] for a thorough description. A brief overview of the soil and contaminant properties is provided here.

Ground soil usually contains three main constituents: solid soil particles (having a dielectric constant between 4.5 and 5.5), air-filled pores, and water. Soils are classified according to the percentages of the three primary components it contains: silt, clay and sand. These components are categorized according to particle size. The dielectric properties of soil vary immensely, depending on the geographic location, particle size and moisture content. Usually, dry soil has very low conductivity. However, the amount of moisture in the soil greatly alters its electrical properties. Due to the high dielectric constant of water, the presence of moisture in soil considerably slows down the propagation of EM propagation in ground. Also, in many cases water has very high conductivity. Thus, EM waves are severely attenuated by the presence of moisture. This results in the depth of penetration decreasing significantly with increase in the moisture content of the soil.

The majority of hydrocarbon contaminants have very low conductivity and can essentially be considered lossless. The dielectric constant of these contaminants usually falls between 1.5 and 6. In many cases, these contaminants take one of the two shapes: they either form a downward plume that gradually mixes in the soil and spreads out, or they make a well-defined plume flowing sideways. In the presence of a well-defined water-table, this plume floats on the water-soil interface due to its immiscibility with water.

We have developed a general-purpose GPR simulator, capable of predicting the radar returns for a variety of soil and target models. Due to the large variation in soil properties and expected targets, we have concentrated on analyzing several canonical models. These models, although not exhaustive in number, do provide information on the ability of GPR in accessing contamination sites.

For the simulations presented in this report, one of three soil models was used: (1) a homogeneous ground; (2) a ground having a well-defined water-table such that there is an

abrupt change in the dielectric constant of ground at the soil-water interface and; (3) a ground with dielectric constant increasing linearly with depth to model a gradual increase in the moisture content of soil with depth. For an inhomogeneous ground, the soil was modeled as a stratified (planarly layered) medium, with the permittivitty of each individual layer being constant.

All material media, including soil, are characterised by three electromagnetic parameters: the permeability, permitivity and conductivity. The effect of these parameters can by accounted for by calculating the Green's function for the media. A Green's function physically represents the fields generated in the media due to a unit source. The Green's function plays the same role as the system impulse response in system theory.

Due to the wide varations in soils and subsurface objects throughout the country, it is not possible to run simulations on all combinations of soils and targets. Because of this we have limited the number of soil models to three, and consider four canonical targets in this investigation. A discription of the target and soil models are presented later in the report.

Recently a computer code has been developed by researchers for EPRI that predicts immiscible contaminant transport in subsurface systems [2]. This PC-based program, called VALOR, uses a two-dimensional, finite-difference technique to model the flow equations for contaminants. VALOR predicts the flow of the contaminant in any given soil for which the soil and contaminant properties are given. We have recently received the documentation for the software, and plan to use this code to model the contamination flow in soil for future work.

B. GROUND-PENETRATING RADAR SIMULATOR

An important part of our development of ground target identification algorithms has been a GPR simulator that is capable of predicting the radar returns of realistic objects. The development of such a simulator is a challenging problem in itself, since the wave equations that predict the evolution of the incident and reflected fields are complex vector equations. Also, the ground itself complicates matters, since it is a large, penetrable object that must be modeled correctly.

Problems of this sort are called forward-scattering electromagnetic problems, since the transmitted fields and the object are known. A number of techniques exist for solving

forward electromagnetic problems. Of these, we chose the finite-difference time-domain (FDTD) technique for our GPR simulator. This technique has been used extensively since the early 1980's to solve a wide range of electromagnetic problems and has a number of attractive features for solving electromagnetic scattering problems. The most important feature for our purposes is that it is not encumbered by the presence of dielectrics in either the target or the background medium (the ground, in our case). Since the ground is an important factor in the nature of the radar returns, this is a most attractive feature.

In the sections that follow, we outline the basic aspects of the FDTD technique. This will be followed by a description of the capabilities of our FDTD code and the presentation of simulated radar returns calculated by this code.

a. The Finite-Difference Time-Domain Technique

The FDTD technique was developed in 1966 by Kane Yee [3], but it was not until the mid 1970's that computer storage capabilities had risen to the level necessary to solve useful problems. Since that time, FDTD has become one of the most popular numerical techniques used for time-varying electromagnetic problems and has been the subject of numerous papers and books [4-7].

The FDTD technique follows directly from Maxwell's equations, which are the fundamental equations that relate the electric and magnetic fields, **E** and **H**, respectively, to the current and charges that ultimately cause them. In differential form, Maxwell's equations read:

$$\nabla \mathbf{x} \mathbf{E} = -\mu \frac{\partial \mathbf{H}}{\partial t} \tag{1}$$

$$\nabla \mathbf{x} \mathbf{H} = \mathbf{J} + \varepsilon \frac{\partial \mathbf{E}}{\partial t}, \tag{2}$$

where $\mathbf{J} = \sigma \mathbf{E}$ is the current density, measured in amperes per square meter, and μ, ε and σ are scalar parameters called the permeability, permitivity and conductivity of the medium. Also, $\nabla \mathbf{x}$ is called the curl operator, which, in Cartesian coordinates, operates on vectors according the formula

$$\nabla \mathbf{x} \mathbf{E} = \left[\frac{\partial E_z}{\partial y} - \frac{\partial E_y}{\partial z}\right] \hat{\mathbf{a}}_x + \left[\frac{\partial E_x}{\partial z} - \frac{\partial E_z}{\partial x}\right] \hat{\mathbf{a}}_y + \left[\frac{\partial E_y}{\partial x} - \frac{\partial E_x}{\partial y}\right] \hat{\mathbf{a}}_z , \tag{3}$$

where E_x, E_y, and E_z are the x, y, and z components of the vector **E**, respectively, and $\hat{\mathbf{a}}_x$, $\hat{\mathbf{a}}_y$, and $\hat{\mathbf{a}}_z$ are unit vectors in the x, y, and z directions, respectively. According to (1) and (2), the time derivative of **H** is controlled by the curl of **E**, whereas the time derivative of **H** is controlled by both the curl of **E** and the current density at that point.

The FDTD technique starts by dividing a three-dimensional region of space into rectangular cells, as shown in Figure 1. Each cell is numbered according the indices (I,J,K) along the x, y, and z axes, respectively, and have dimensions Δx, Δy, and Δz along the x, y, and z axes, respectively. Within each cell, the six possible components of the **E** and **H** fields are sampled at distinct points in time. Figure 2 shows the field points within each cell. As can be seen, the **E** and **H** fields are interlaced in space, which makes it possible to perform the curl operations efficiently.

A system of six difference equations for the six components of the electric and magnetic fields can be obtained by evaluating the time and space derivatives numerically. To accomplish this, electric fields are sampled at integer multiples of the time step, $t = n\Delta t$, where Δt is the time step. Conversely, the magnetic fields are sampled half integer multiples of the time step, $t = (n+\frac{1}{2})\Delta t$. As an example, the equation for the x component of the magnetic field at $t = (n+\frac{1}{2})\Delta t$ is:

$$H_x^{n+1/2}(I,J,K) = H_x^{n-1/2}(I,J,K) + \frac{\Delta t}{\mu}\left\{\frac{1}{\Delta y}\left[E_z^n(I,J,K) - E_z^n(I,J+1,K)\right]\right.$$

$$\left. + \frac{1}{\Delta z}\left[E_y^n(I,J,K+1) - E_y^n(I,J,K)\right]\right\}. \qquad (4)$$

As can be seen, the new value of the H\S\do5(x) at $t = (n+\F(1,2))\Delta t$ depends upon the previous value of H_x at $t = (n-\frac{1}{2})\Delta t$, as well as the values of two nearby E field components at H_x at $t = n\Delta t$. Using equations like this, the sample values of the H field components at one point in time can be calculated from E and H field sample values at previous points in time. Similar equations can be derived for each component of the E field in terms of previously calculated E and H field values.

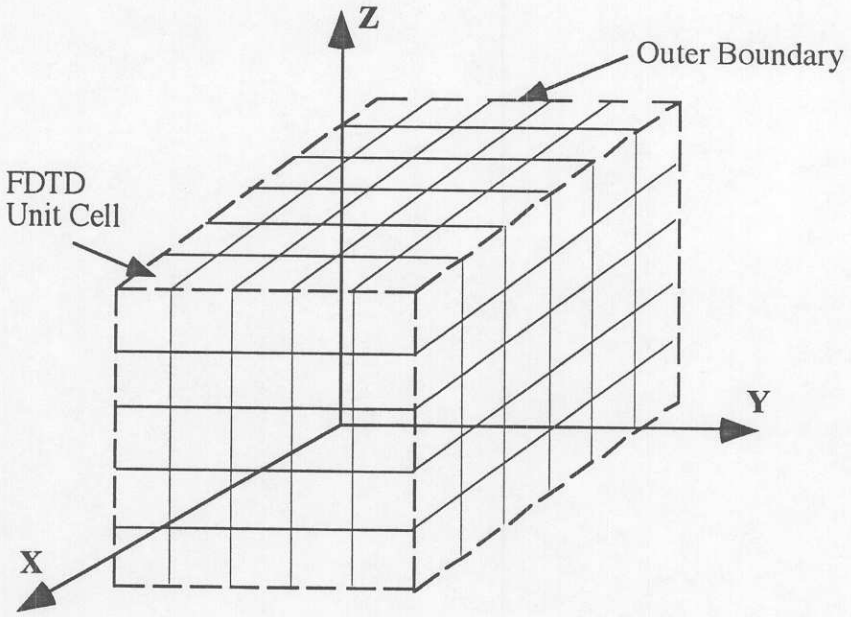

Figure 1. A rectangular FDTD numerical grid.

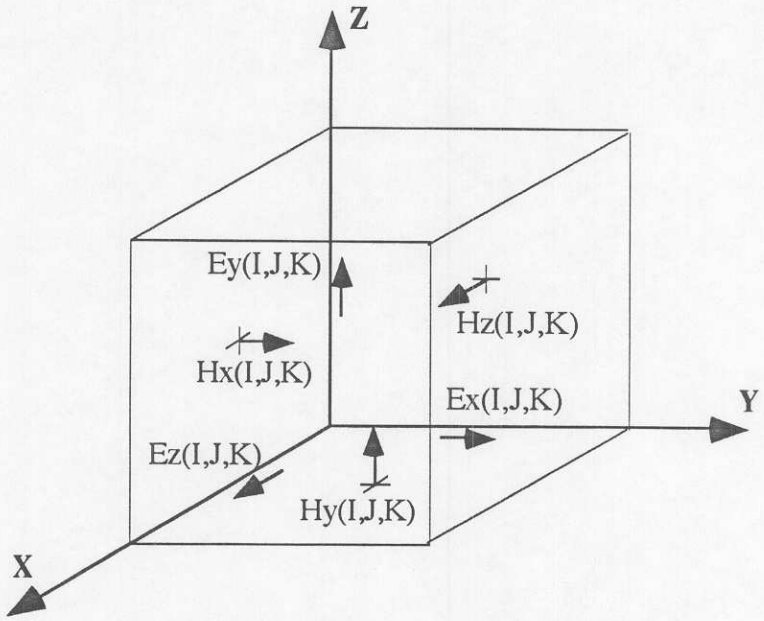

Figure 2. The FDTD unit cell showing the electric and magnetic field evaluation points.

Using these field advance equations, the general FDTD technique proceeds by sequentially evaluating the magnetic fields over the entire solution space and then the electric fields at the next half-time step. This "leapfrog" process is repeated for the entire time history of the waveforms, producing time-marching solutions of the fields within the solution space. This procedure describes the basic FDTD field-advance algorithm. However, in order to perform useful calculations, several other issues must be addressed. These include the specification of the object, the incident fields, and the field-advance equations at the edges of the solution space.

To specify the object, all that is necessary is to specify the appropriate material parameters (ε, μ, and σ) in each cell where the object appears. Since the cells are rectangular, the object that is specified is a "stairstep" equivalent of the actual object. As long as the cell size is small, the errors incurred by this stairstep approximation are minor. The properties of the ground are specified in exactly the same way-on a cell-by-cell basis.

The incident fields can be specified in a number of ways, depending upon the nature of the source and where it is located. If the source is a known current distribution (such as a line source) that is relatively close to the scatterer , the time history of these currents can be added to the curl-H equation (2) and forced directly in the field-advance equations. On the other hand, for sources that are distant from the object, the incident field is usually a plane wave and is known *a-priori*. For this case, the FDTD solution space is divided into two regions. The region immediately surrounding the object is called the total field region, where the fields calculated by the code are the total fields, which are defined as the sum of the incident fields plus the fields scattered (i.e., reflected) by the object. The region that surrounds the total field region is called the scattered field region, and only the field actually scattered by the object is calculated. Dividing the fields in this way allows the fields close to the outer boundary of the solution space to be outward propagating, which is necessary in order to reduce nonphysical, numerical reflections at this boundary.

Another issue involves the outer boundary of the solution space. The problem here is that the standard FDTD field advance equations require a knowledge of the fields surrounding a point. This knowledge is not possible at the outer boundary, since fields beyond this boundary are not stored. As a result, other means of advancing these fields must be used. These techniques are called absorbing boundary conditions, since they absorb the outward propagating waves without causing nonphysical, numerical reflections. Although a number of techniques have been devised, the most popular one is one developed by Mur [8], which

uses the electromagnetic wave equation to estimate the magnitude and propagation direction of the fields near the outer boundary and, from these, calculates the fields along the outer boundary. This technique is often augmented with an additional correction scheme developed by Fang [9]. Using these techniques, numerical reflections from the outer boundary are typically -30 dB down from the amplitude of the incident fields.

Finally, even though the FDTD technique calculates fields in the time domain, steady state field amplitudes can be obtained easily. This is accomplished by recognizing that the time-domain waveforms are the convolution of the incident field waveform and the system transfer function. Hence, we can obtain the steady state response at any frequency simply by taking the Fourier transform of a given waveform and dividing it by the Fourier transform of the incident field waveform. In this way, the response due to a steady state source of any frequency can be obtained from a single time-domain calculation.

b. The University of Kansas FDTD Code

The FDTD computer code used in our investigation was developed as an outgrowth of the FDTD code development that has been an ongoing activity at the Radar Systems and Remote Sensing Laboratory at The University of Kansas for the past ten years [10]. In order to model the specific geometries needed for this project, several modifications were made to our existing code. Most of these modifications were related to the presence of the ground, and the antenna sources used to illuminate the targets.

Since our target identification study dealt with two-dimensional geometries, our FDTD code was specialized to model two-dimensional fields. As is well known in electromagnetic theory, fields that do not vary along an axis (say, the z axis) can be divided into two separate classes. The first is called TE fields, which consist of three components: E_x, E_y, and H_z. The second class consists of TM fields, which also have three components: H_x, H_y, and E_z. Hence, a two-dimensional FDTD code only needs to deal with three field components at a time, rather than six. This is a significant simplification. The determining factor of whether the fields are TE or TM depends upon the nature of the source. For the electric line source transmitting antennas used in our studies, the fields are always TM.

Figure 3 shows a schematic of a typical GPR in a monostatic set-up. Here, the antennas, object, and ground are all drawn inside a rectangular, two-dimensional FDTD cell

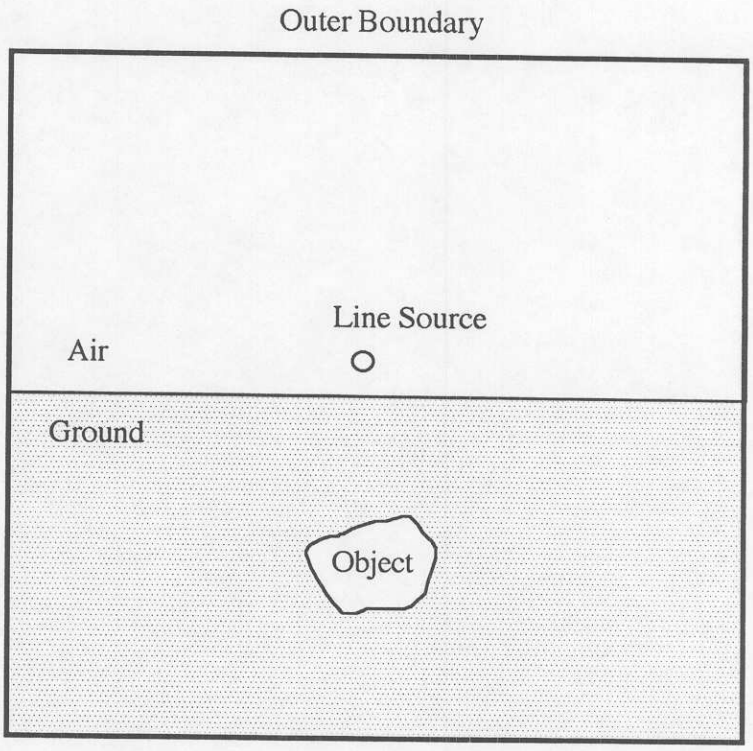

Figure 3. Typical monostatic GPR set-up.

space. The source of the incident fields is a wire current (i.e., line source), located just above the ground interface. The cells that contain the ground are shown with light shading, and the object is shown with heavy shading. At the outer boundary of the FDTD cell space, the absorbing boundary conditions are invoked numerically to close the cell space. Since the incident fields are generated close to the object, there is no need of a total field/scattered field boundary, and total fields are calculated in each cell of the cell space.

The first choice to be made when running the FDTD code is to choose the cell size. In general, the smaller the cell size chosen, the more cells are necessary to model the scatterer and the surrounding ground. A small cell size increases the computational accuracy but also increases the computational resources, since more cells are needed and a smaller time step must be used. Another consideration is that the cell dimensions can be no larger than roughly 1/10 of the smallest wavelength component present in the transient waveforms. Hence, the cell size must be chosen carefully in terms of the object size and the transient waveform used to describe the incident fields.

Limitations of the maximum object size that can be analyzed by this (or any other FDTD) code are set by the available memory. Simply stated, the memory requirements of a two-dimensional code grow in direct proportion to the total number of cells used in the FDTD lattice. At present, our code runs on a Sun Sparc 10 workstation, with 96 megabytes of random access memory. With this machine, we can analyze a cell space up to 100x100 square meters for a radar frequency of 150 megahertz without using virtual memory.

Our code is capable of modeling both homogeneous grounds and stratified grounds. If future investigations were to require that the ground vary along the horizontal axis, appropriate modifications to the code could be easily implemented (at the cost, however, of increased computational resources). Also, both lossy and lossless grounds can be modeled. This is accomplished simply by choosing the correct value of the permitivity ε (measured in farads per meter) and conductivity σ (measured in semans per meter) for each cell.

Once the material parameters of each cell are fixed in the code (including the air, ground, and object), a time waveform is chosen for the current flowing on the line-source antenna. This current controls the incident field and is chosen so that this field has frequency components that fall within the range of interest. Usually, it is best for this waveform to have no DC component so that the very low frequency components of the incident field are small enough to allow the absorbing boundary condition to work well (since the outer boundary must be several wavelengths from the scattering object).

c. Simulated Radar Returns

In this section we present typical results from the FDTD GPR simulator. As mentioned earlier in the report, a GPR can be operated in one of two modes: (1) monostatic, in which the transmit and recieve antennas are colocated, and (2) bistatic, in which case the two antennas are separated. For the simulations presented in this section, we limit the mode of operation to the monostatic mode, which was selected because this is the mode most often used in the field. As discussed later in the image generation section, the bistatic mode provides much more information about the target. Therefore, the bistatic mode is used for image generation.

The geometry of the GPR simulation is shown in Figure 4. Here, a monostatic radar traverses along the ground above the object. As it traverses, it emits pulses with its transmitting antenna, and receives echoes from its receiving antenna. When these pulse amplitudes are plotted vs. the delay time and the radar position, a series of lines are obtained that indicate how the strength of the echo varies. Plots like these are commonly called pulse-echo plots.

We now present several pulse-echo profiles, Figures 5 through 8, which illustrate the resolution capabilities of a GPR system. The object considered in the pulse-echo profile of Figure 5 is a rectangular, dielectric cylinder with $\varepsilon_r = 6.0$ and 0.5 m sides is buried a distance $d = 3.7$ m below the surface of a homogeneous, lossless ground with $\varepsilon_r = 3.0$. The transmitted pulse is a 24 nsec doublet, which has the same shape as the bottom horizontal trace in this pulse-echo plot. As can be seen from each line in this plot, the received waveforms are also doublets, since there is only a single target. However, the relative delay of these waveforms are functions of the radar position, and the minimum delay is obtained when the radar is directly over the object.

The object considered in the pulse-echo profile of Figure 6 consists of two rectangular cylinders buried side by side, each with the same characteristics as in Figure 5. These cylinders are separated by 2 m and are buried 4.7 m below the ground surface and the radar pulse width is again 24 nsec. This example illustrates the cross-range resolution of the GPR. When the radar is at a position of 1m or 8m, the two extreme values, the received waveform clearly displays two targets. However, when the radar is located midway between the targets at a position of 4m, the returns from the two targets arrive at the radar at the same time. At this position the radar cannot resolve the two targets. By looking at the entire pulse-echo profile, however, it is possible to tell that two targets are buried at the same depth.

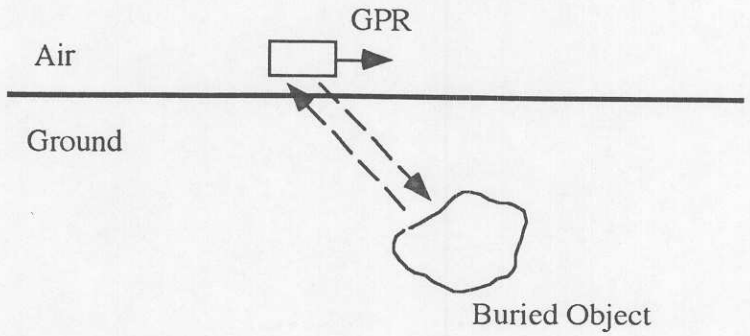

Figure 4. A schematic diagram of the FDTD GPR simulator.

The object considered in the pulse-echo profile of Figure 7 consists of the same two cylinders, this time buried on top of each other. This example demonstrates the radar's range resolution capabilities. The first is 2.5 m from the surface, and the second is 4.5 m from the surface. For this case, the received time signals clearly show the presence two pulses. The first is due to the shallow target and the second is the response of the deeper cylinder.

Finally, the object considered in Figure 8 bears similarities to the previous two objects. Here, two cylinders are buried side by side at different depths. The pulse-echo plot for this case contains effects of both their vertical and lateral displacements, but the vertical displacement is most readily seen by the eye. Two separate returns are clearly identifiable between positions 1m to 6m. However, beyond 6m the distance to both targets is approximately the same. The returns from both targets arrive at the radar at the same time and the radar no longer can resolve them.

Once we developed the capability of accurately predicting the radar returns for a GPR system, our next task was to process the simulated data and generate subsurface images. The pulse-echo profiles that are typically used to display GPR data become very complicated for heterogeneous soils with multiple targets. The purpose of image processing is to generate accurate maps or subsurface profiles. These maps can then be used in the site cleanup process. In the following section, we introduce two techniques for generating these images.

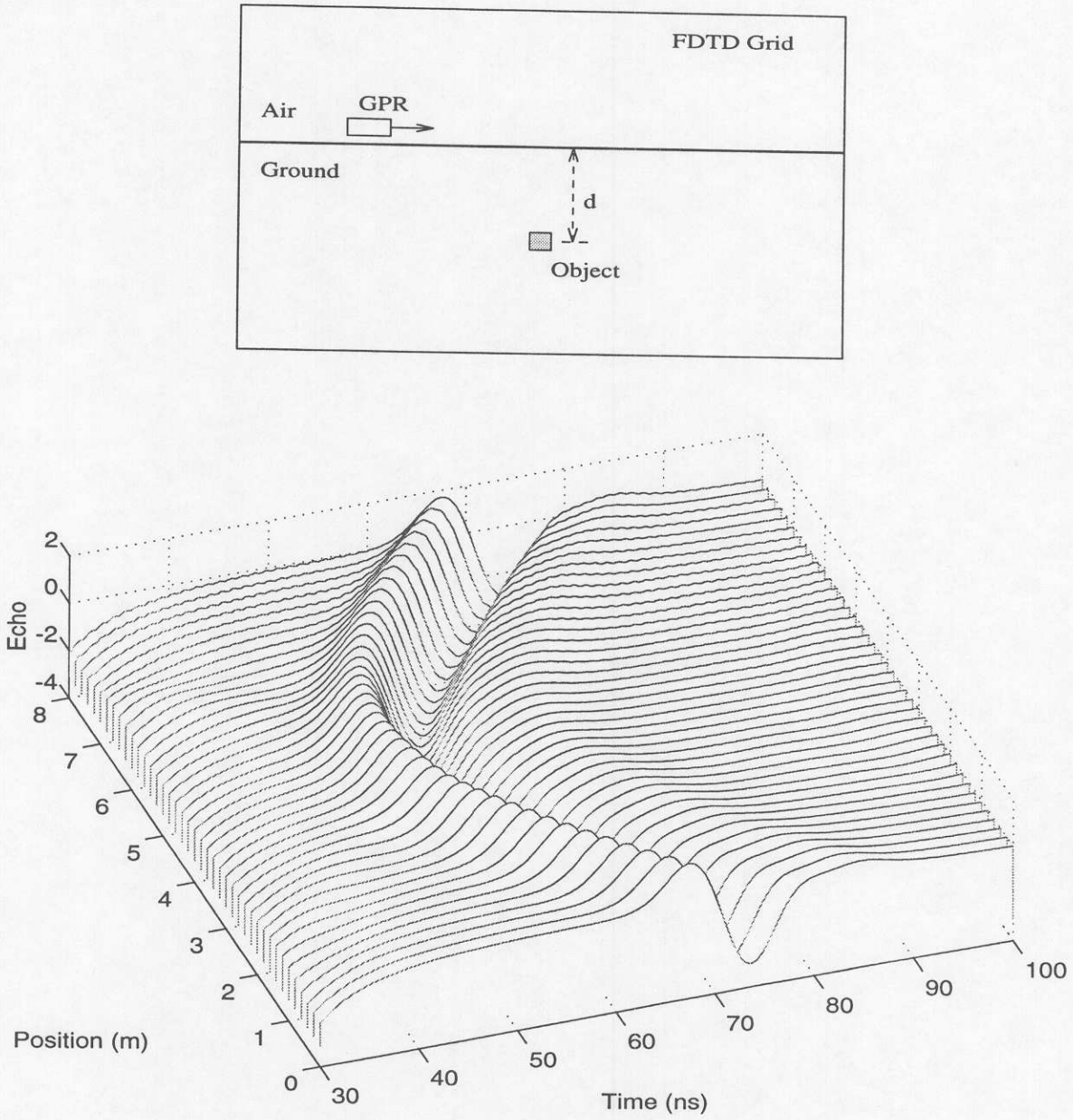

Figure 5. A pulse-echo profile of a single underground point object.

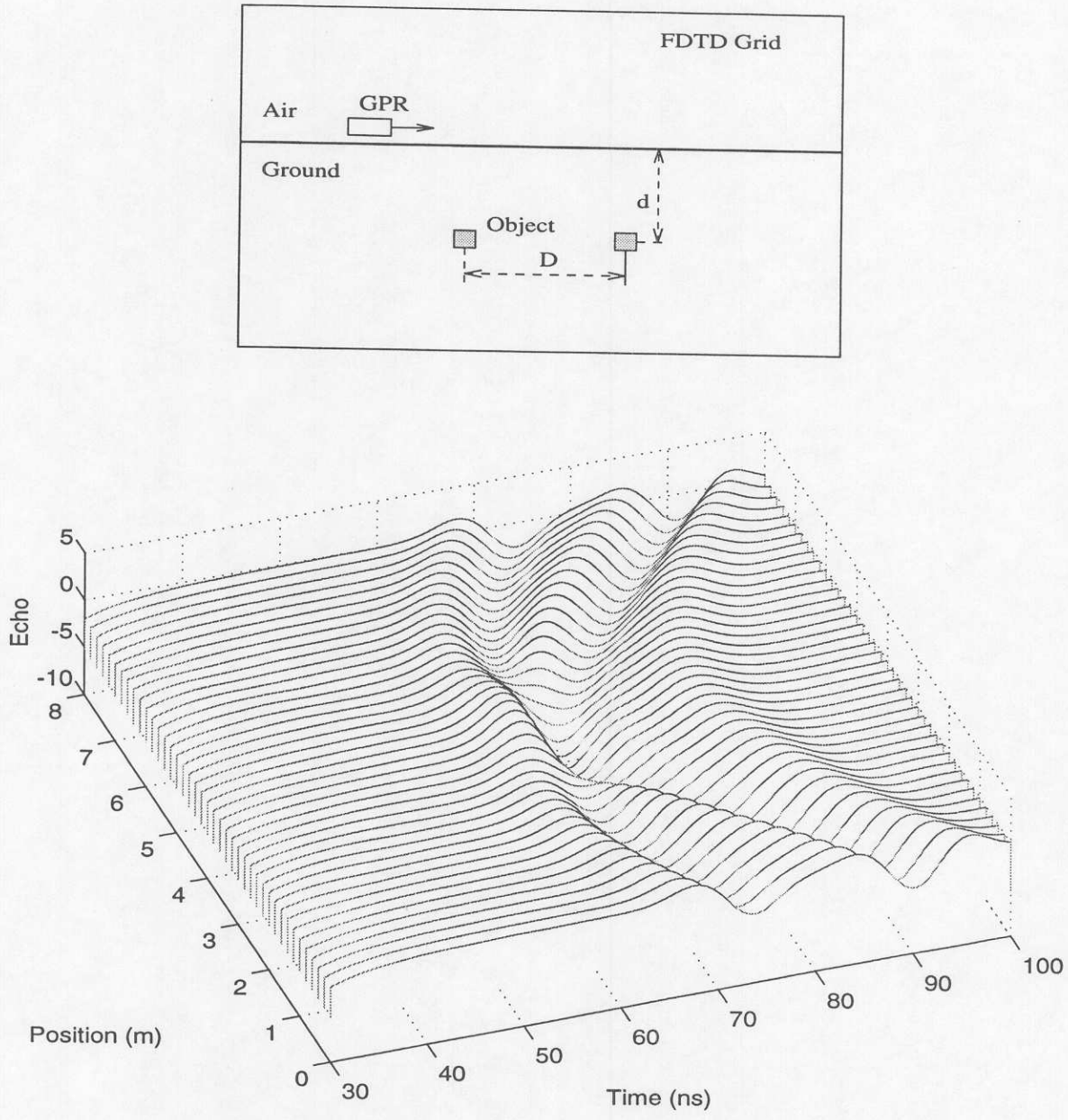

Figure 6. A pulse-echo profile of two horizontal underground point objects.

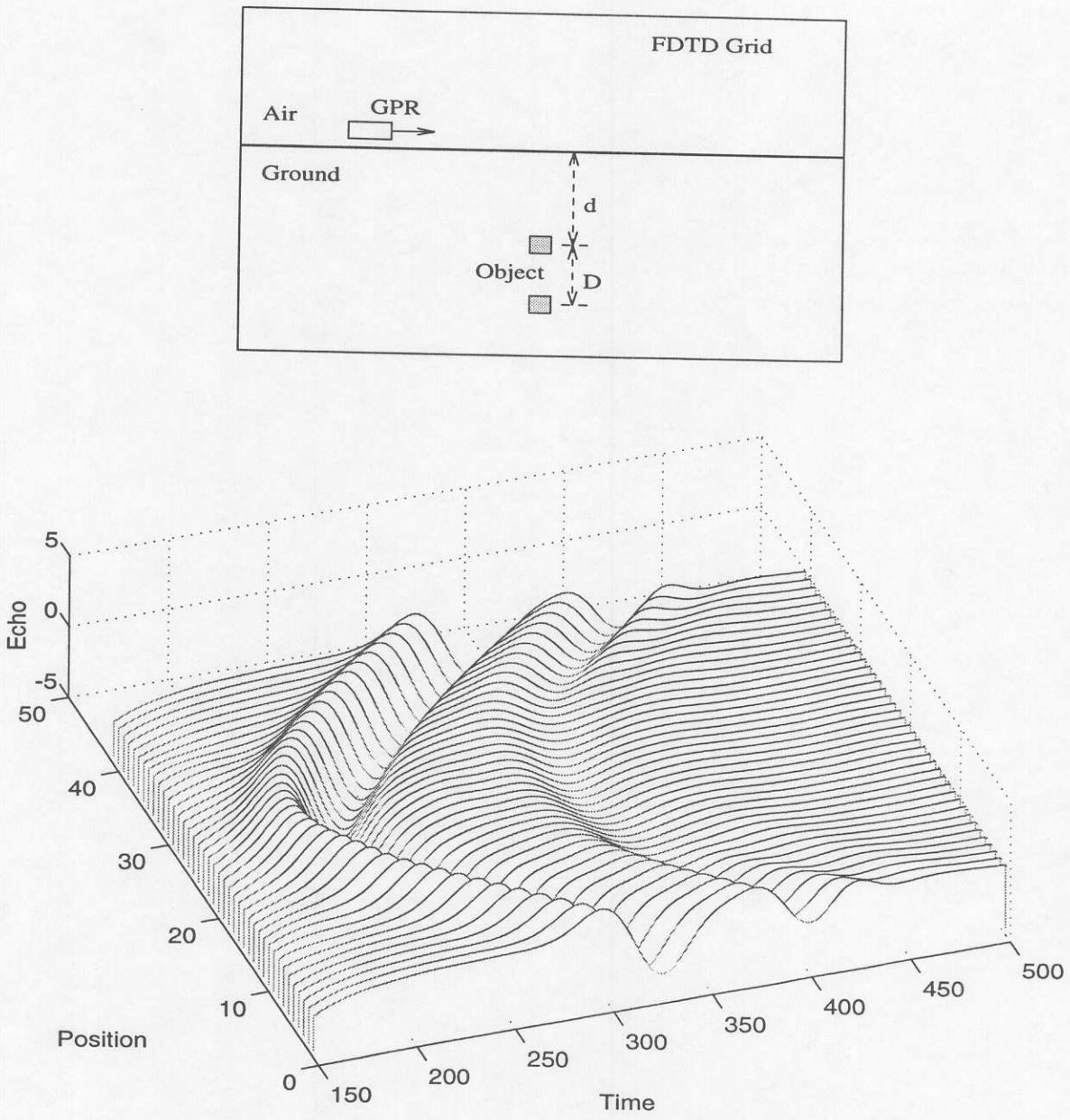

Figure 7. A pulse-echo profile of two vertical underground point objects.

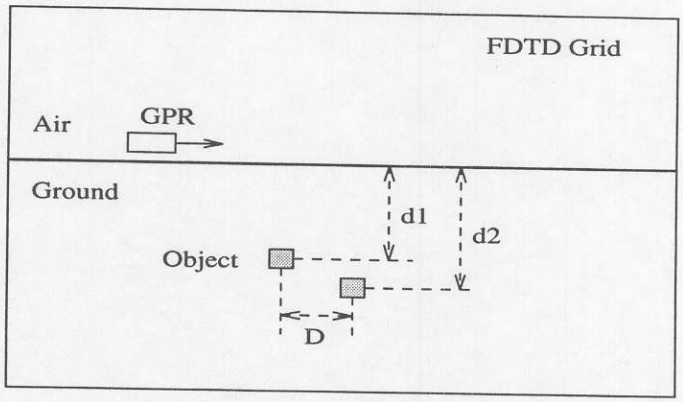

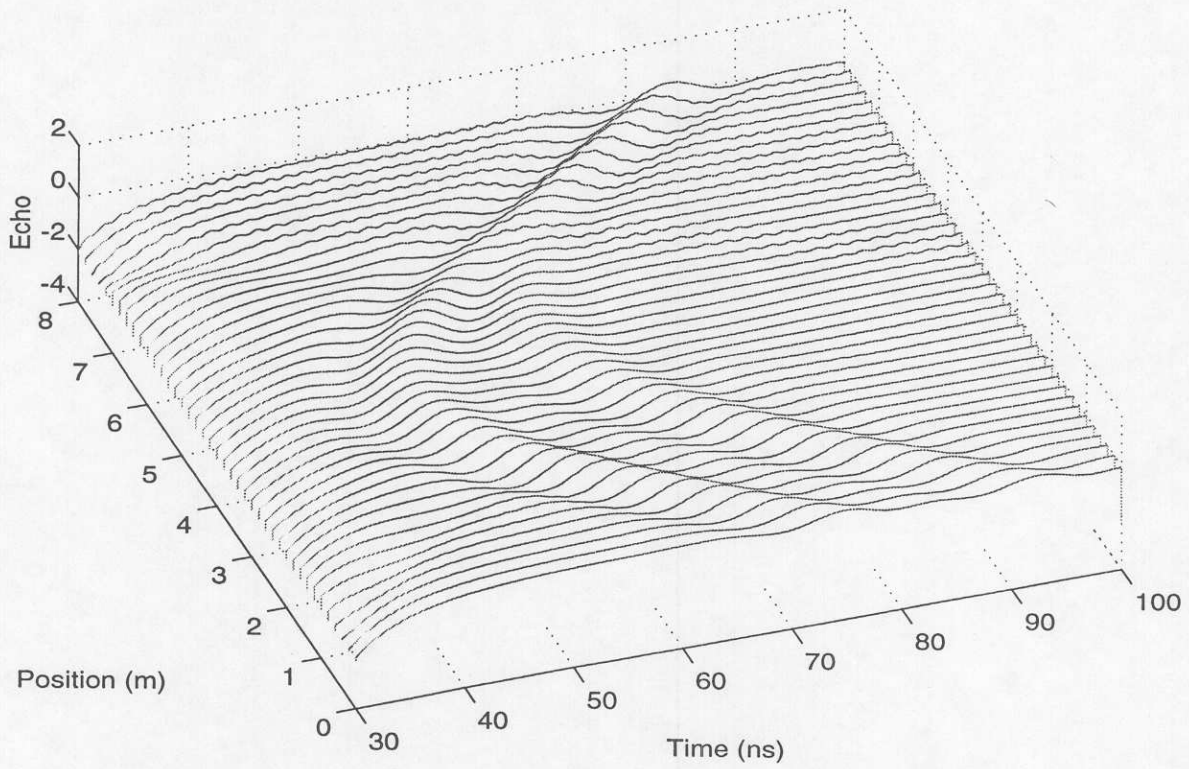

Figure 8. A pulse-echo profile for two underground point objects.

C. SUBSURFACE IMAGING

The goal of an inversion algorithm is to generate subsurface images from measured data. Inversion techiques fall into two general groups: those that attemp to locate and define the object boundaries and those that attemp to construct an object profile. In addition to providing location and boundaries, the object profile also provides estimates of the object's constitutive parameters. Among the techniques used to located the object and its boundaries are synthetic aperture imaging [11] and microwave holography [12, 13]. Techniques that are useful in generating object profiles are diffraction tomography [14-16] and the iterative Born technique [17]. An excellent review of most of these techniques is provided in [18]. In this investigation, we concentrated on obtaining estimates of object profiles from GPR data. More information is obtained on the target if both its boundaries and constitutive parameter are known. This additional information is useful in automatic target classifications algorithms, which are discussed later in the report.

The techniques for image reconstruction fall under a broader class of problems generally known as the electromagnetic (EM) inverse sacttering problems. In an inverse problem, the incident and the scattered fields are known, and the objective is to reconstruct some physical properties of the target. For the imaging techniques investigated here, the goal is to recover the permittivitty profile of the object from the scattered electric fields. The measurements of the fields are available only at points external to the object. Since an infinite number of objects can produce the same fields at a finite number of points outside the object, the solution to inverse problems is inherently non-unique.

Several techniques are available for solving EM inverse scattering problems. A majority of these technques are based on linearizing the problem through a weak scattering assumption. Under this assumption, the scattered field is assumed to be small compared to the incident field. Tomography and constrained optimization-based techniques are two of the most popular methods of solving the inverse problem using linear approximations. The latter technique can also be applied iteratively to solve a nonlinear problem. Application of both of these techniques for subsurface imaging are presented in this section.

a. Formulation of the Inverse Problem

Consider the geometry of the two-dimensional problem depicted in Figure 9. The geometry consist of two half-spaces characterized by the constitutive parameters $\{\mu_0 , \varepsilon_1\}$

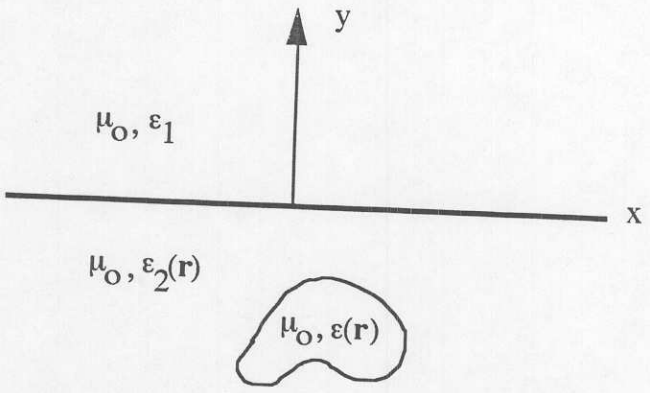

Figure 9. Two-dimensional geometry for inverse scattering formulation.

and $\{\mu_0, \varepsilon_2(\mathbf{r})\}$. Region 1 is a homogeneous half-space and corresponds to free space. Region 2, representing the ground, is an inhomogeneous half-space. An inhomogeneous scattering object of finite size with permeability and permittivity μ_0, $\varepsilon(\mathbf{r})$ is located in region 2. Our goal is to generate an image of the scatterer by solving the inverse scattering problem. We follow a procedure similar to that in [17] by developing an integral equation for the object profile.

The total field $\phi(\mathbf{r})$ satisfies the scalar wave equation,

$$\{\nabla^2 + k^2(\mathbf{r})\}\phi(\mathbf{r}) = q(\mathbf{r}) \tag{5}$$

where $q(\mathbf{r})$ are the sources and the wave number is given by

$$k^2(\mathbf{r}) = \begin{cases} \omega^2\mu_0\,\varepsilon_1 & \mathbf{r} \in \text{Region 1} \\ \omega^2\mu_0\,\varepsilon_2(\mathbf{r}) & \mathbf{r} \in \text{Region 2} \\ \omega^2\mu_0\,\varepsilon(\mathbf{r}) & \mathbf{r} \in \text{scatterer} \end{cases} \tag{6}$$

For TM polarization the total field, $\phi(\mathbf{r})$, represents the z-component of the electric field. Define a background wave number corresponding to the half-space problem with the scattering target absent as

$$k^2_b(\mathbf{r}) = \begin{cases} \omega^2 \mu_0 \varepsilon_1 & \mathbf{r} \in \text{Region 1} \\ \omega^2 \mu_0 \varepsilon_2(\mathbf{r}) & \mathbf{r} \in \text{Region 2} \end{cases} \tag{7}$$

Adding and subtracting $k^2_b(\mathbf{r})$ to (5) results in

$$\{\nabla^2 + k^2_b(\mathbf{r})\}\phi(\mathbf{r}) = q(\mathbf{r}) - O(\mathbf{r})\phi(\mathbf{r}) \tag{8}$$

where the object profile $O(\mathbf{r})$ is defined as

$$O(\mathbf{r}) = k^2(\mathbf{r}) - k^2_b(\mathbf{r}) \tag{9}$$

By introducing a Green's function $g_b(\mathbf{r}, \mathbf{r}')$ that satisfies the equation

$$\{\nabla^2 + k^2_b(\mathbf{r})\}g_b(\mathbf{r}, \mathbf{r}') = -\delta(\mathbf{r} - \mathbf{r}'), \tag{10}$$

the solution for the total field $\phi(\mathbf{r})$ can be expressed as

$$\phi(\mathbf{r}) = -\int d\mathbf{r}'[q(\mathbf{r}') - O(\mathbf{r}')\phi(\mathbf{r}')]g_b(\mathbf{r}, \mathbf{r}'). \tag{11}$$

The incident field produced by the sources in the absence of the scatterer is

$$\phi_{inc}(\mathbf{r}) = -\int d\mathbf{r}' q(\mathbf{r}')g_b(\mathbf{r}, \mathbf{r}'). \tag{12}$$

Therefore (11) becomes

$$\phi(\mathbf{r}) = \phi_{inc}(\mathbf{r}) + \int d\mathbf{r}' O(\mathbf{r}')\phi(\mathbf{r}')g_b(\mathbf{r}, \mathbf{r}') \tag{13}$$

Since the total field is the sum of the incident and scattered fields and the scattered field is the only field containing information about the object, (13) is re-written as

$$\phi_{sca}(\mathbf{r}) = \int d\mathbf{r}' O(\mathbf{r}')\phi(\mathbf{r}')g_b(\mathbf{r}, \mathbf{r}') \qquad (14)$$

The total field inside the scatterer is a function of the object profile making (14) a nonlinear integral equation of the first kind in $O(\mathbf{r})$. In its present form, (14) is difficult to use in solving for the object profile because the inverse problem is ill posed [19, 20] and inherently non-unique by virtue of the equivalence principle.

During the course of this investigation, we examined two different techniques for generating subsurface images: diffraction tomography and constrained optimization or regularization. Diffraction tomography is an extension of medical x-ray tomography and accounts for diffraction effects resulting from the use of low frequency signals. Constrained optimization is a technique that allows incorporation of *a-prior* information of the object in the image-generation process. In the following sections, we discuss these two techniques and outline their strengths and weaknesses.

b. Image Generation by Diffraction Tomography

Tomography may be loosely defined as a process of reconstructing an object's image from projection measurements made around the object. Projections are a measure of the effect the object has on the applied electromagnetic field. Using this technique, an N-dimensional object, which is represented by its N-dimensional Fourier transform, can be reconstructed from the (N-1)-dimensional Fourier transforms of its projections [14-16]. The basis for imaging with tomography is provided by the projection-slice theorem. This theorem states that for an N-dimensional object, the (N-1)-dimensional Fourier transform of the measured projections along a line are mapped into a slice of the N-dimensional spatial Fourier transform of the object. By measuring projections along lines surrounding the object, the Fourier transform space of the object is filled out. The next step is to invert the N-dimesional spectral data. The applications of tomography can be broadly classified into two major areas; X-ray tomography and diffraction tomography.

Computer tomography has been applied to medical imaging for several years. The field of medical, or X-ray, tomography has been well studied. In medical applications, high energy X rays are used in reconstructing an image. Because of the high frequencies used, diffraction effects are neglected, and the straight-ray models work reasonably well. Using these models, the Fourier transform of the field along a direction perpendicular to the direction of the incident wave gives the Fourier transform of a slice of the object along this direction according to the projection slice theorem as shown in Figure 10. By rotating the transmitter and the receiver 360 degrees around the object, a sufficient number of measurements can be made, and the object can be reconstructed from these slices.

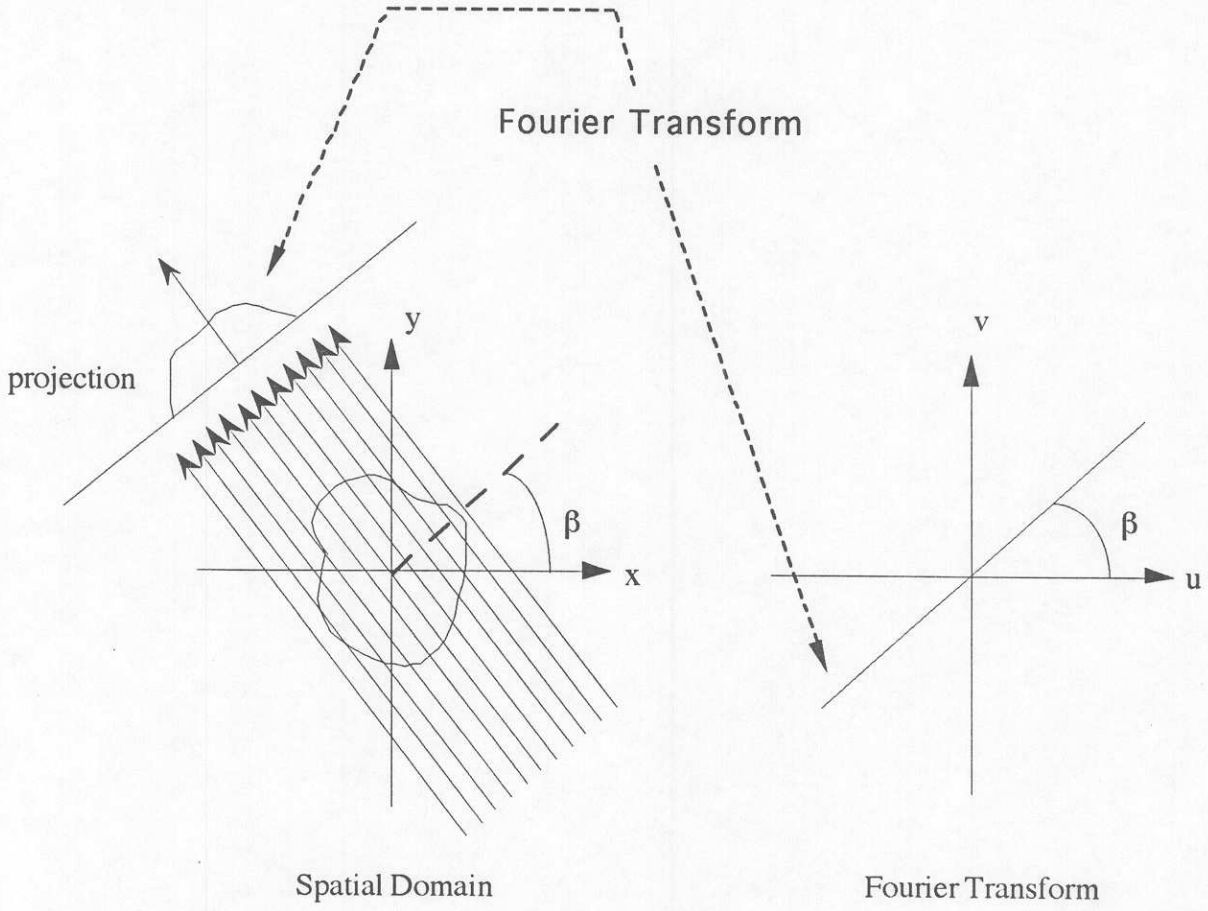

Figure 10. The projection slice theorem in medical tomography.

The application of tomographic techniques to geophysical problems is relatively new. In geophysical applications, low frequency electromagnetic waves must be used due to the high attenuation suffered by higher frequencies. When the wavelength of an incident wave is close in size to the scattering objects, differaction effects play a dominant role. A diffraction-corrected version of tomography, called diffraction tomography, accounts for these effects as is used in subsurface applications.

Diffraction tomography is the generalization of X-ray tomography. In this technique, diffraction effects are incorporated to account for the lower frequencies used. For diffraction tomography, a result similar to the projection slice theorem of medical tomography is utilized to reconstruct the image of the object from the one-dimensional Fourier transforms of the field. This can be stated as follows: the two-dimensional Fourier transform of the object along a semicircular arc is related to the one-dimensional Fourier transform of the scattered field measured along a straight line tangential to the arc as shown in Figure 11. The image is reconstructed by taking the projections of the object for several angles of incidence.

Once the spectrial domain data of the object profile is obtained, an inversion algrothim is required to get the data back into the object space. One of the most popular algorithms used in diffraction tomography is the backpropagation algorithm proposed by Devaney [14]. This algorithm reconstructs the object by using a spatial filter to propagate the fields backward into the object from the receivers. A direct interpolation scheme has also been used by some people to solve similar problems [21]. In this technique, the object is reconstructed by interpolating the Fourier transform of the object onto a rectangular grid and then using the standard inverse Fourier transform techniques to recover the object pofile. Although the concept behind the direct interpolation is simple, interpolation onto a rectangular grid requires a complicated coordinate transformation. The backpropagation algorithm was used for the work presented here. The formulation of diffraction tomography and the backpropagation algorithm are discussed in detail the seond and third quarterly reports for this project [28, 29].

The biggest advantage of diffraction tomography is its simplicity and elegance. The well-developed concepts of Fourier transform and other signal processing tools are used in this technique to reconstruct the object. Diffraction tomography provides a computationally fast and efficient method of solving the inverse problems. For these reasons, this technique was investigated in the first part of this project.

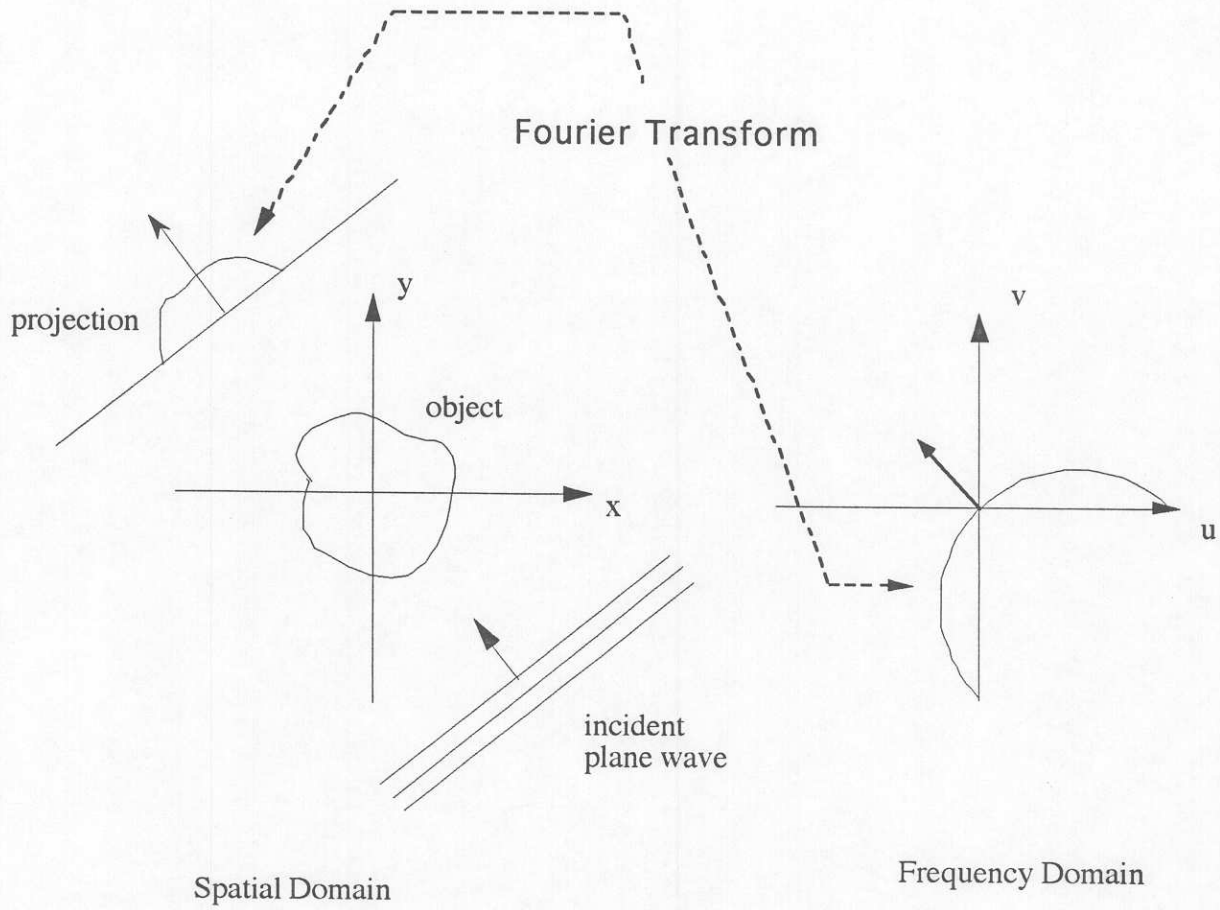

Figure 11. The relationship between Fourier transforms of the object and the scattered field for diffraction tomography.

However, the various assumptions used in the development of diffraction tomography limit its applicability in many subsurface imaging applications. A major limitation of the technique is the inherent assumption of weak scattering. This limits the maximum constrast between the object and the background material, as well as the overall size of the object. A second limitation is the fact that the reconstructed image is inherently a low-pass version of the original object. Thus, sharp transitions and finer features of the object are lost in the reconstruction process. The biggest limitation of diffraction tomography in imaging shallow subsurface objects is the assumption of a homogeneous background. This assumption,

although valid for deeply buried objects, greatly limits the application of the technique for generating accurate images.

Most of limitations associated with diffraction tomography can be overcome by using a technique based on constrained optimization. For this reason, a constrained optimization-based technique was investigated and developed during the latter portion of this project. The details of this technique are now presented.

c. Image Generation by Constrained Optimization

The general inverse scattering problem, as mentioned ealier, is an ill-posed problem. One technique used in solving ill-posed problems is regularization. Regularization, or constrained optimization, is based on replacing the ill-posed problem with one that is well posed. We use a general Tikhonov regularization procedure to obtain the object profile [20]. Rather than solving the problem

$$\mathcal{A}O = d, \tag{15}$$

the Tikhonov procedure solves the problem of minimizing $\| \mathcal{A}O - d \|^2$, under the constraint $\| \mathcal{L}O\|^2$= constant, where $\mathcal{L}$ is a suitably chosen linear stabilizer and $\|\bullet\|^2$ is the l_2 norm. An equivalent statement of this procedure is [22]

$$\min \{\| \mathcal{A}O - d \|^2 + \mu^2 \| \mathcal{L}O \|^2\} \tag{16}$$

where μ is called the smoothing parameter. The larger the value of μ the smoother the image while smaller values of μ generate higher fidelity images. In the above equations $\mathcal{A}$ is the operator in (14), O is the object profile, and d is the scattered field data ϕ_{sca}. The solution of (16) is [22]

$$O = (\mathcal{A}^*\mathcal{A} + \mu^2 \mathcal{L}^*\mathcal{L})^{-1} \mathcal{A}^* d \tag{17}$$

The selection of the stabilizer $\mathcal{L}$ is arbitrary and is required because of the small eigenvalues of $\mathcal{A}$ in (15). The stabilizer increases the eigenvalues of the system to the point were the system is no longer ill posed. The selection of $\mathcal{L}$, along with the smoothing

parameter, dictates the degree of smoothness in the solution. A good overview on selecting a stabilizer is provided by Twomey [19].

Equation (17) can be solved numerically by a discretization of the problem. This is done by first dividing the region of space into pixels and then expanding the object profile into a set of N expansion functions of the form

$$O(\mathbf{r}) = \sum_{n=1}^{N} a_n f_n(\mathbf{r}) \tag{18}$$

where a_n are unknown constant coefficients and the expansion functions $f_n(\mathbf{r})$ are given by

$$f_n(\mathbf{r}) = = \begin{cases} 1 & \mathbf{r} \in n^{th} \text{ pixil} \\ 0 & \text{elsewhere} \end{cases} \tag{19}$$

Using (19) in (14) and assuming the field remains constant over each expansion function results in

$$\phi_{sca}(\mathbf{r}) = \sum_{n=1}^{N} a_n \phi(\mathbf{r}') \int d\mathbf{r}' f_n(\mathbf{r}') g_b(\mathbf{r}, \mathbf{r}') \tag{20}$$

If a total of M receiver-transmitter pairs are used, (20) may be put into matrix form as

$$[A]O=D \tag{21}$$

where D is a M-element column vector containing the measured data, O is an N-element column vector containing the unknown coefficients and [A] is an NxM matrix whose elements are given by

$$A_{ij} = \phi(\mathbf{r}') \int_{i} g_b(\mathbf{r}_j, \mathbf{r}') \, d\mathbf{r}' \tag{22}$$

The regularized solution for the object profile is

$$O= (A^*A+ \mu^2 L^*L)^{-1} A^*d \tag{23}$$

In our solution we use a first difference stabilizer L, which requires a certain degree of smoothness in the first derivative of the object profile [19].

Solutions to the inverse problem require evaluation of an integral of the background Green's function over each pixel as given by (22). The appropriate Green's function for GPR work depends upon the soil characteristics and the placement of the recievers. Consider the half-space problem depicted in Figure 12. A transmitter is located in region 1, which represents free space, while a scattering object is placed in region 2 representing the soil. Receivers may be placed either on the air-to-soil interface or down a borehole. Let the receiver location and an observation point inside the scatterer be denoted by $\mathbf{r'} = \mathbf{a}_x x' + \mathbf{a}_y y'$ and $\mathbf{r} = \mathbf{a}_x x + \mathbf{a}_y y$, respectively. If the soil is modeled as a homogeneous half-space and if the receiver is located in region 1, the desired Green's function is

$$g_b(\mathbf{r}, \mathbf{r'}) = \int_{-\infty}^{+\infty} \frac{T(\lambda)}{2u_1} e^{u_2 y - u_1 y'} e^{j\lambda(x - x')}\, d\lambda \qquad (24)$$

whereas if the receiver is located in region 2, the Green's function is

$$g_b(\mathbf{r}, \mathbf{r'}) = \int_{-\infty}^{+\infty} \frac{1}{2u_2} [e^{u_2 (y - y')} + R(\lambda)\, e^{u_2 (y + y')}] e^{j\lambda(x - x')}\, d\lambda \qquad (25)$$

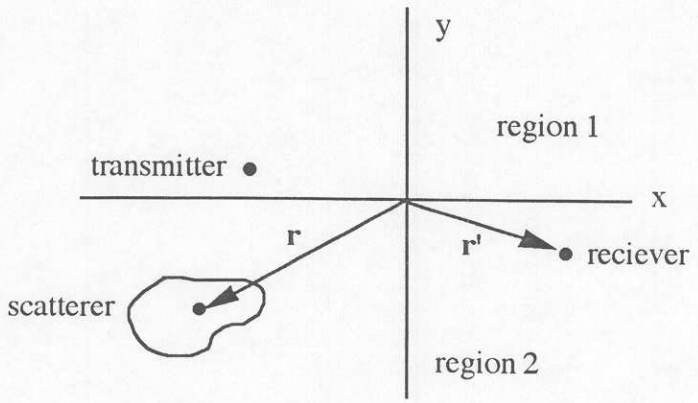

Figure 12. Line source located above a dielectric interface.

Equations (24) and (25) represent plane-wave spectra where $T(\lambda)$ in (24) is the transmission coefficient from region 1 to region 2 and $R(\lambda)$ in (25) is the reflection coefficient in region 2 from of the air-to-soil interface.

Direct evaluation of (24) or (25) using the plane-wave spectrum formula for the Green's function is not practical. It can be seen from these expressions for the Green's function that it cannot be evaluated in closed form in either case. Furthermore, the permittivitty of medium 2 in (25) is higher than the permittivitty of medium 1. Thus, this expression is difficult to deal with when the angle of incidence becomes larger than the Brewster angle. But when a predominant wavenumber can be separated from the rest of the spectrum, and the angle of incidence for this predominant wavenumber is not too large, simplified expressions for the Green's function are obtained as

$$g_b(\mathbf{r}, \mathbf{r}') \approx \frac{1}{j4} T(\Lambda)\, H_0^{(2)}(k_1 |r_1|) \tag{26}$$

for receivers on the surface, and

$$g_b(\mathbf{r}, \mathbf{r}') \approx \frac{1}{j4} [H_0^{(2)}(k_1 |r_1|) + R(\Lambda)\, H_0^{(2)}(k_1 |r_2|)] \tag{27}$$

for the receiver locations in the borehole. Here Λ is the predominant wavenumber, r_1 is the distance between the points (x,y) and (x',y'), and r_2 is the distance between (x,y) and (x',-y').

Unfortunately, the assumption of small angles of incidence is not valid for many cases in the imaging problem since the receivers need to be spread out for better angular coverage of the object. Thus, some other technique for the evaluation of the Green's function is needed for use in the inverse problem.

Instead of evaluating the Green's functions analytically in (24) and (25), the Green's functions may be obtained numerically by utilizing FDTD and a Fourier transform. Once the Green's function is evaluated, its integral over each cell in the object is evaluated numerically by assuming its variation within a cell to be linear. We use this technique of evaluating the integral of the Green's function for the work presented in this paper.

d. Image Generation by the Born Iterative Technique

In this section we develop a solution for the object profile based on the Born iterative technique. The Born iterative method requires successive solutions to the forward scattering problem followed by the inverse scattering problem. The forward scattering problem is solved using FDTD while a regularized solution is sought for the inverse problem.

The details of the Born Iterative procedure are explained in [17]. Briefly, the technique consists of the following. The object profile is recovered from the measured or simulated radar data by first using a Born approximation. This amounts to a linear solution to the inverse problem and provides good quality images under weakly scattering conditions. The first estimate of the object profile is fed into the FDTD code to update the total field in the scatterer. These fields are substituted back into the inverse scattering problem and (20) is once again inverted using regularization techniques. This iterative process of going back and forth from the forward scattering problem to the inverse scattering problem is repeated until a specified error limit is reached. The error limit is reached when the total field calculated by the FDTD code with update object profile agrees to within a given tolerance level of the measured (simulated) radar data. The solution procedure is depicted in Figure 13.

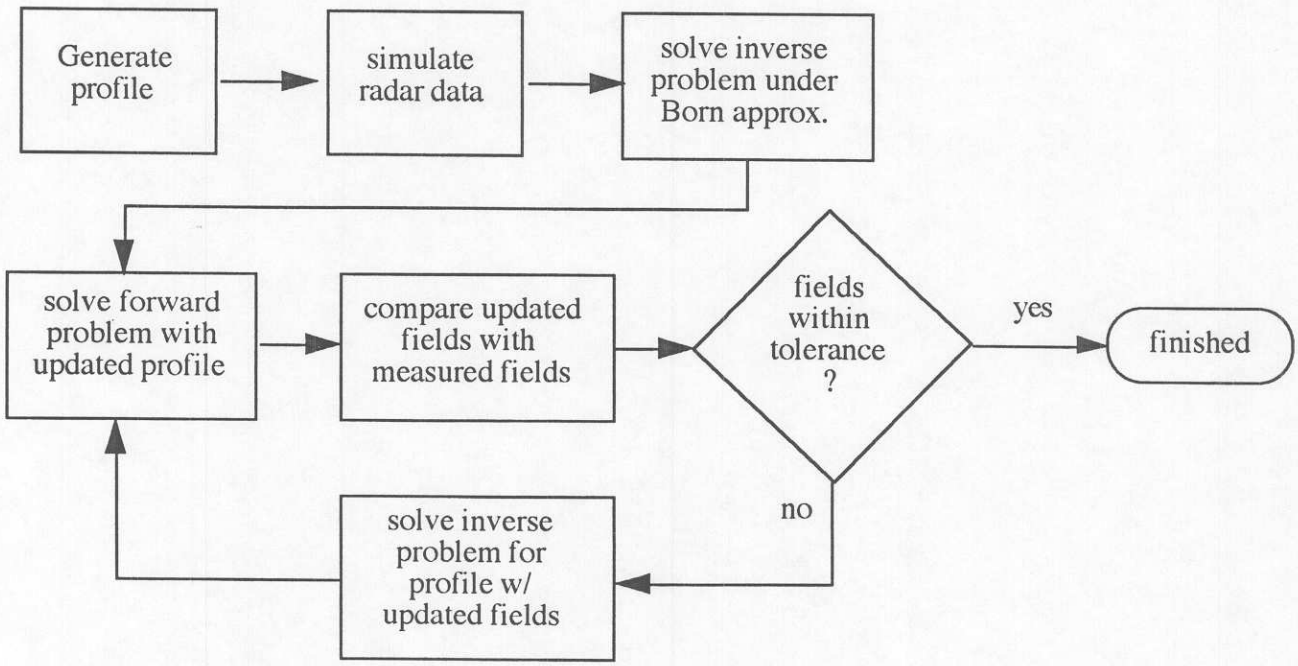

Figure 13. Born iterative scheme for subsurface imaging.

e. Simulations of Subsurface Imaging

In this section we present several two-dimensional simulations of subsurface image generation using constrained optimization and the Born iterative technique. Since it is impossible to perform simulations on all possible combinations of soil profiles and targets, we focused on the various combinations of three soil models and four object configurations. The three soil models are: (1) a homogeneous ground with dielectric constant of 5; (2) a stratified ground where the dielectric constant increases in a linear fashion with depth; and (3) a ground with a discernible water table at a depth of 6.6 m. Illustrations of these models are shown in Figure 14 and their characteristics are tabulated in Table 1. The four object models are: (A) a downward plume with a storage tank; (B) a sideways plume with a storage tank; (C) a downward plume only; and (D) a sideways plume only. These canonical objects are shown in Figure 15.

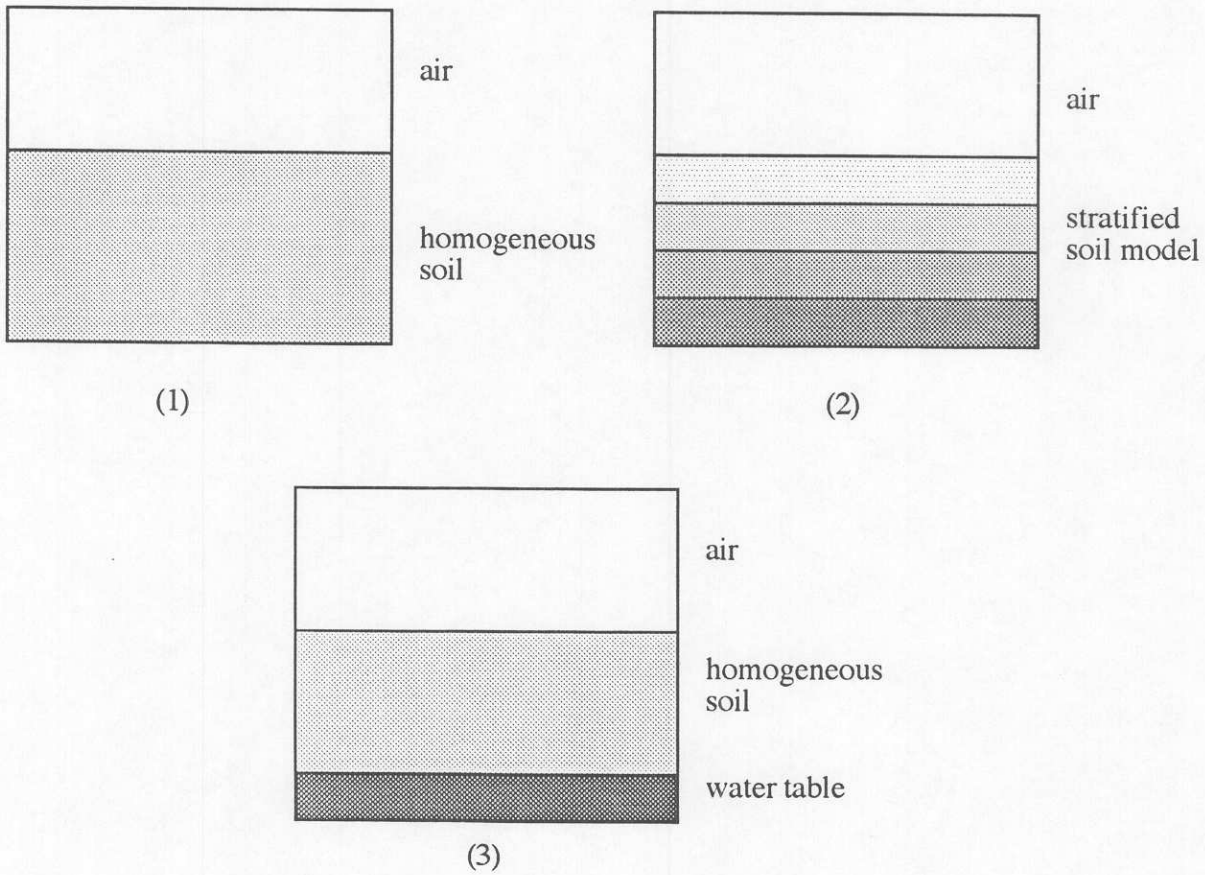

Figure 14. Ground soil models: (1) homogeneous soil; (2) stratified layers; and (3) homogeneous soil with a discernible water table.

Soil Model Number	Characteristics
1	Homogeneous soil with a dielectric constant of 5.
2	Stratified model with 166 layers. Dielectric constant varies linearly from 4 at the top layer to 7 at the bottom layer.
3	A water table located at 6.6 meters. Homogeneous soil above the water table with a dielectric constant of 5.

Table 1. Soil model characteristics.

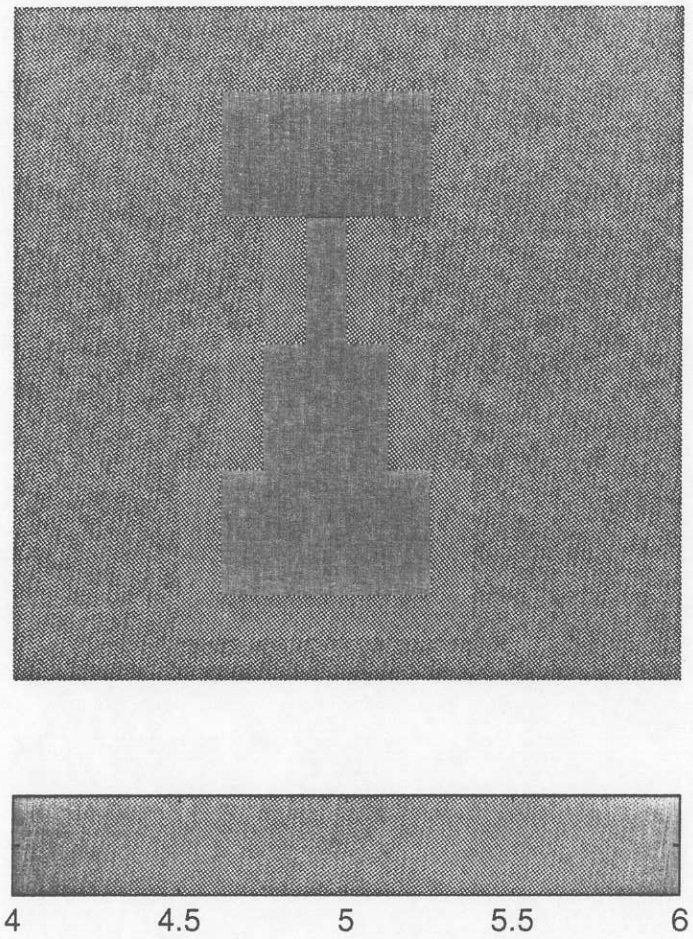

Figure 15a: Target model A.

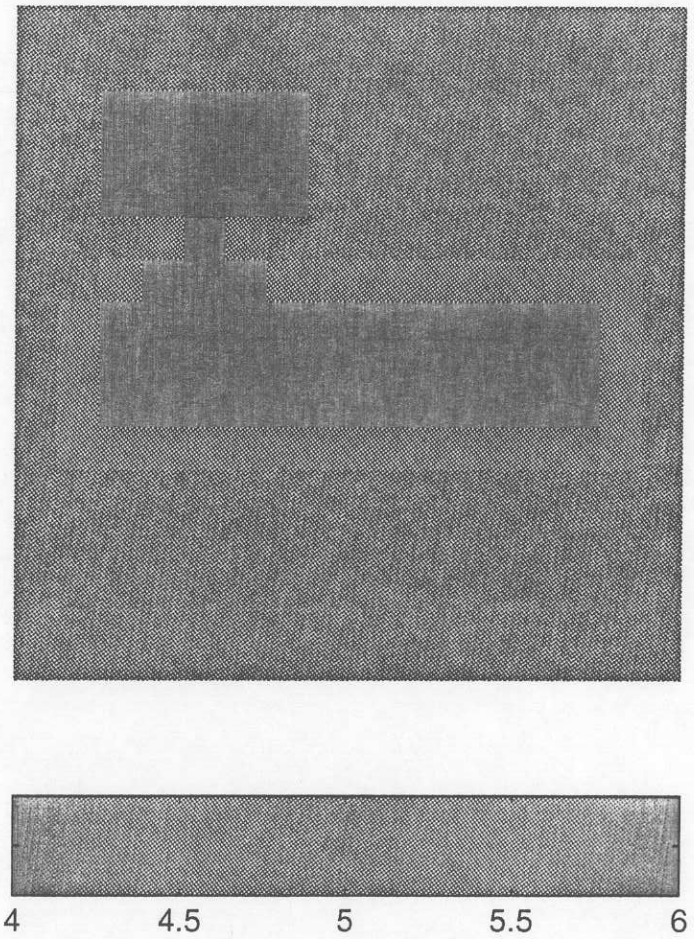

Figure 15b: Target model B.

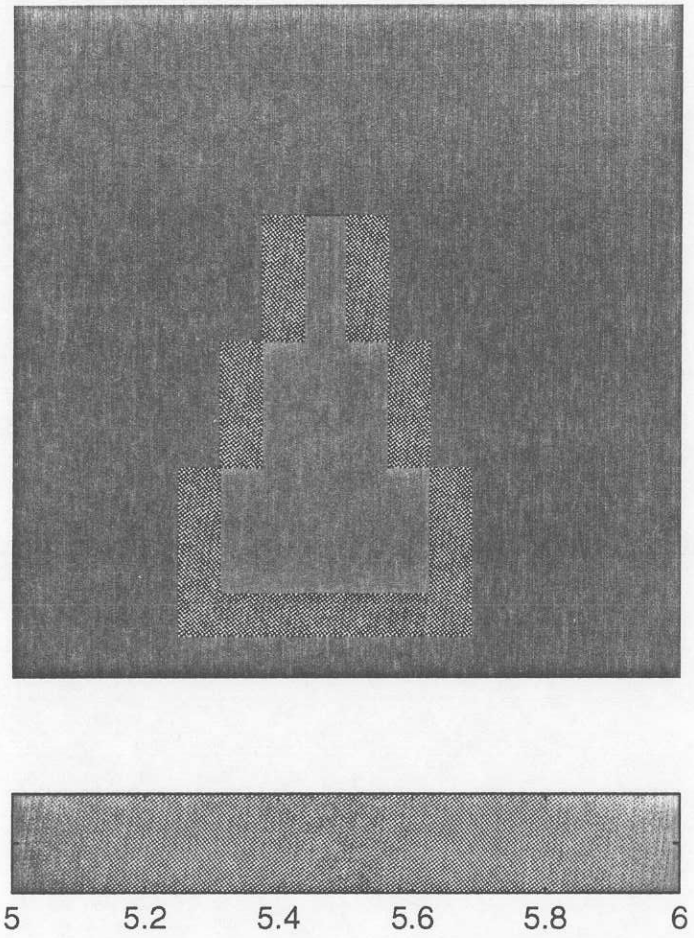

Figure 15c: Target model C.

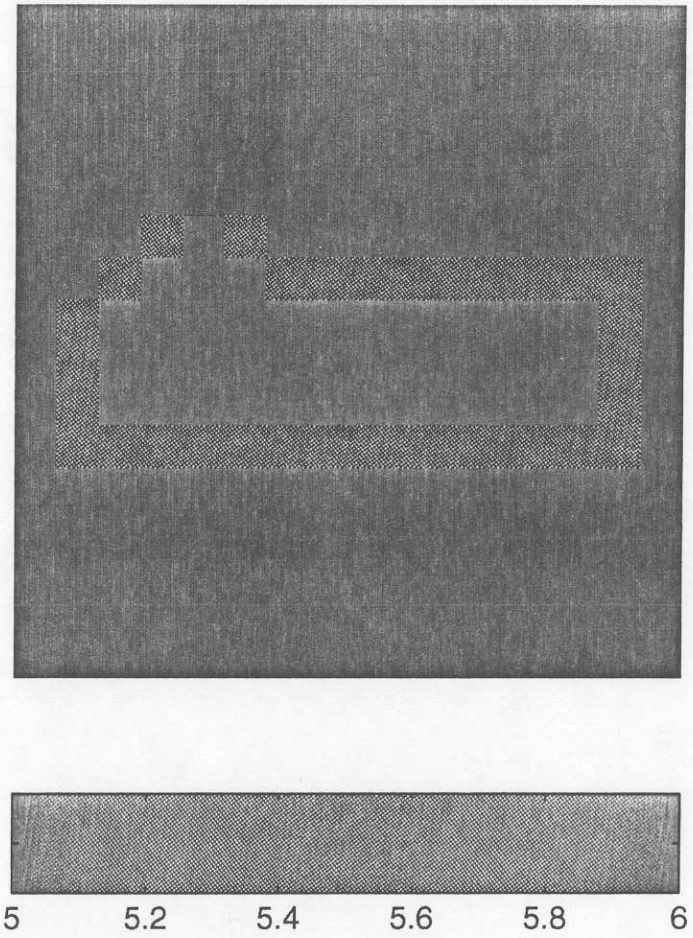

Figure 15d: Target model D.

The geometry of the simulations is depicted in Figure 16. The overall FDTD lattice is 240 cells by 240 cells with free space accounting for the top 40 cells. The object space is limited to a 16-by 16-cell area located inside the FDTD lattice. Images are generated at 75 MHz. Each cell in the lattice is 10 cm and the overall object space is 2.4 x 2.4 meters.

Two different antenna configurations are considered. In the first set-up, both the transmitters and receivers are located on the surface. An off-set VSP is used in the second configuration with the transmitters located on the surface and the receivers located in a vertical borehole. A total of five transmitters, modeled as electric line soures spaced four wavelengths apart, are used in all simulations. Images are generated using the 75 MHz component of the z-directed scattered electric field measured at nine receiver locations for

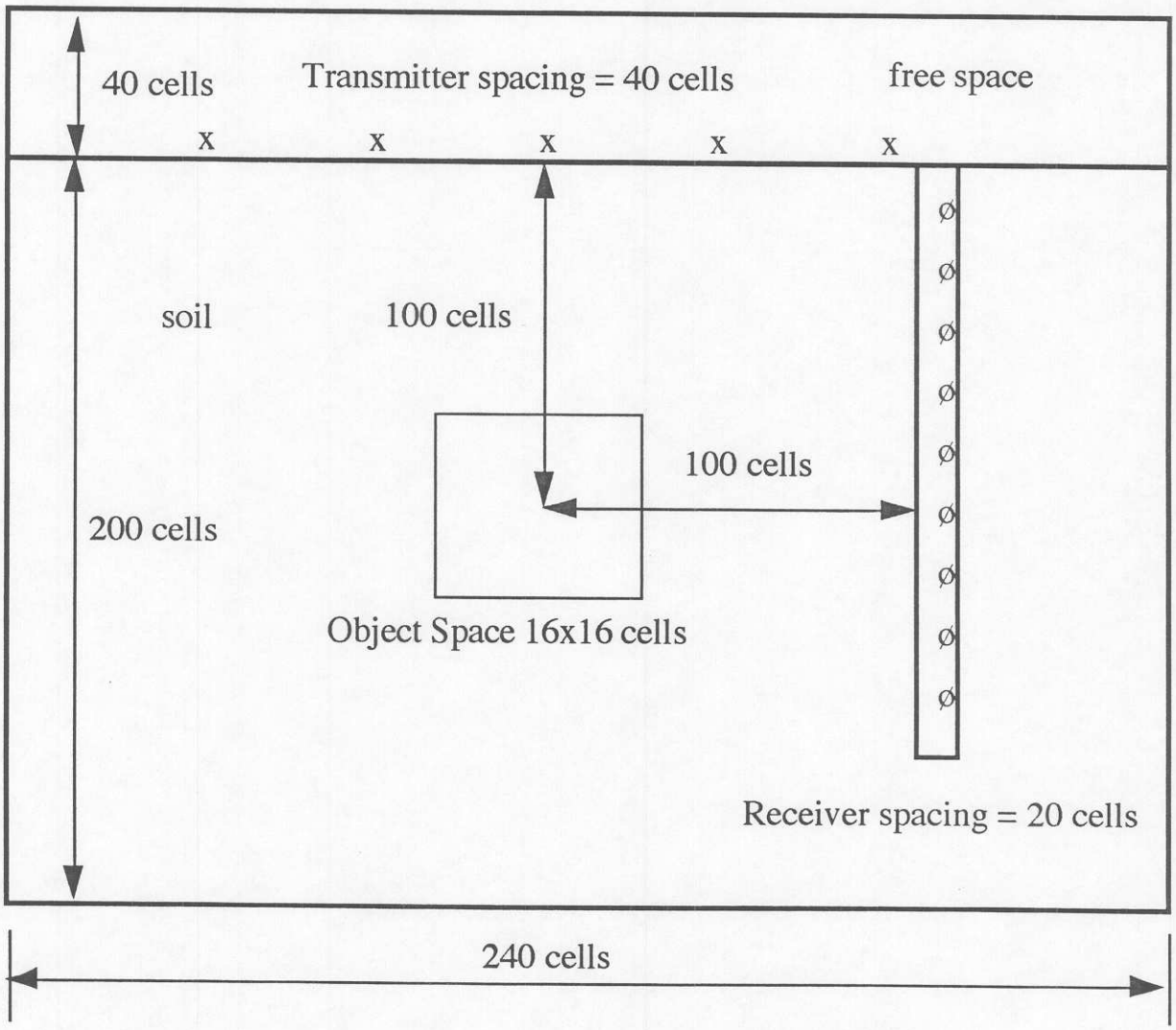

Figure 16. Offset vertical seismic profile GPR simulator geomety.

each transmitter location.

The object space is characterized by 256 unknowns and there are a total of 45 measurements. A quantitative measure of the quality of the reconstructed image is obtained through the root mean-squared error defined as

$$MSE = \sqrt{\frac{\iint_S [\varepsilon_r^{(i)}(\mathbf{r}) - \varepsilon_r(\mathbf{r})]^2 dxdy}{\iint_S [\varepsilon_r(\mathbf{r})]^2 dxdy}} \tag{28}$$

where $\varepsilon_r(\mathbf{r})$ is the true dielectric constant, $\varepsilon_r^{(i)}(\mathbf{r})$ is the reconstructed dielectric constant after the i^{th} iteration, and S is the object space. The root mean-squared error for all the simulations fell in the range of 6% to 11%.

Table 2 list the soil background, target, antenna configuration, and figure number for all the simulations performed in this section. The simulations are grouped into sets to illustrate direct comparisons between various techniques. The first three simulations illustrate the differences when a GPR is operated in the monostatic mode (with no image processing), the bistatic mode with both antennas on the surface and image processing applied, and an offset VSP configuration again with image processing applied. In these simulations a leaking storage tank forming a downward plume buried in homogeneous soil.

In the second set of simulations, Simulation Numbers 4 and 5, the surface-to-surface antenna configuration is compared to an offset VSP configuration for a leaking storage tank forming a sideways plume buried in homogeneous soil. This set of simulations shows that offset VSP offers slightly better resolution compared to when the antennas are placed only on the surface. The third and fourth sets of simulations, Simulation Numbers 6-7 and 8-9, again compare the surface-to-surface antenna configuration to the offset VSP configuration for downward and sideways forming plumes.

The fifth set of simulations, Simulation Number 10-13, are each of the four canonical models buried in inhomogeneous soil with the antennas placed in an offset VSP

Simulation Number	Set	Soil Model	Target	Figure Number	Antenna Placement
1	1	1	A	17	Surface(monostatic)
2		1	A	18	Surface(bistatic)
3		1	A	19	Offset VSP
4	2	1	B	20	Surface(bistatic)
5		1	B	21	Offset VSP
6	3	1	C	22	Surface(bistatic)
7		1	C	23	Offset VSP
8	4	1	D	24	Surface(bistatic)
9		1	D	25	Offset VSP
10	5	2	A	26	Offset VSP
11		2	B	27	Offset VSP
12		2	C	28	Offset VSP
13		2	D	29	Offset VSP
14	6	3	A	30	Offset VSP
15		3	B	31	Offset VSP
16		3	C	32	Offset VSP
17		3	D	33	Offset VSP

Soil Model

1 - Homogenous
2 - Stratified
3 - Water Table

Target Model

A - downward plume with tank
B - sideways plume with tank
C - downward plume only
D - sideways plume only

Table 2. Simulation Test bed.

configuration. This set of four images illustrates that the imaging technique works well even if the background soil is heterogeneous. Provided that the proper background Green's function is selected, the images generated by this technique do not degrade in quality.

The sixth set of simulations, Simulation Number 14-17, again correspond to each of the four canonical models. This time, however, they are buried in homogeneous soil located above a water table. Images were generated with the antennas placed in an offset VSP configuration. This set of simulations again shows that images can be generated even in the presence of a water table.

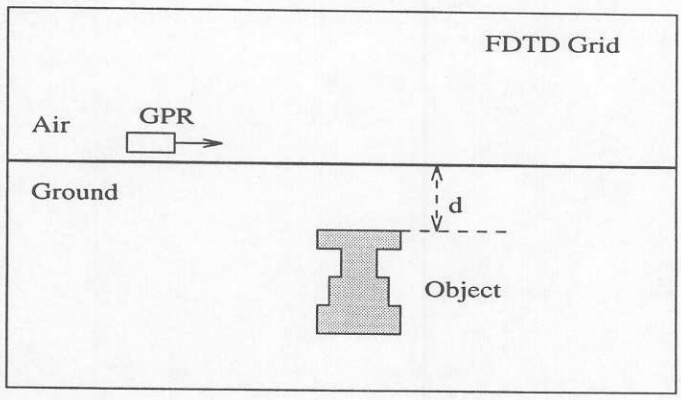

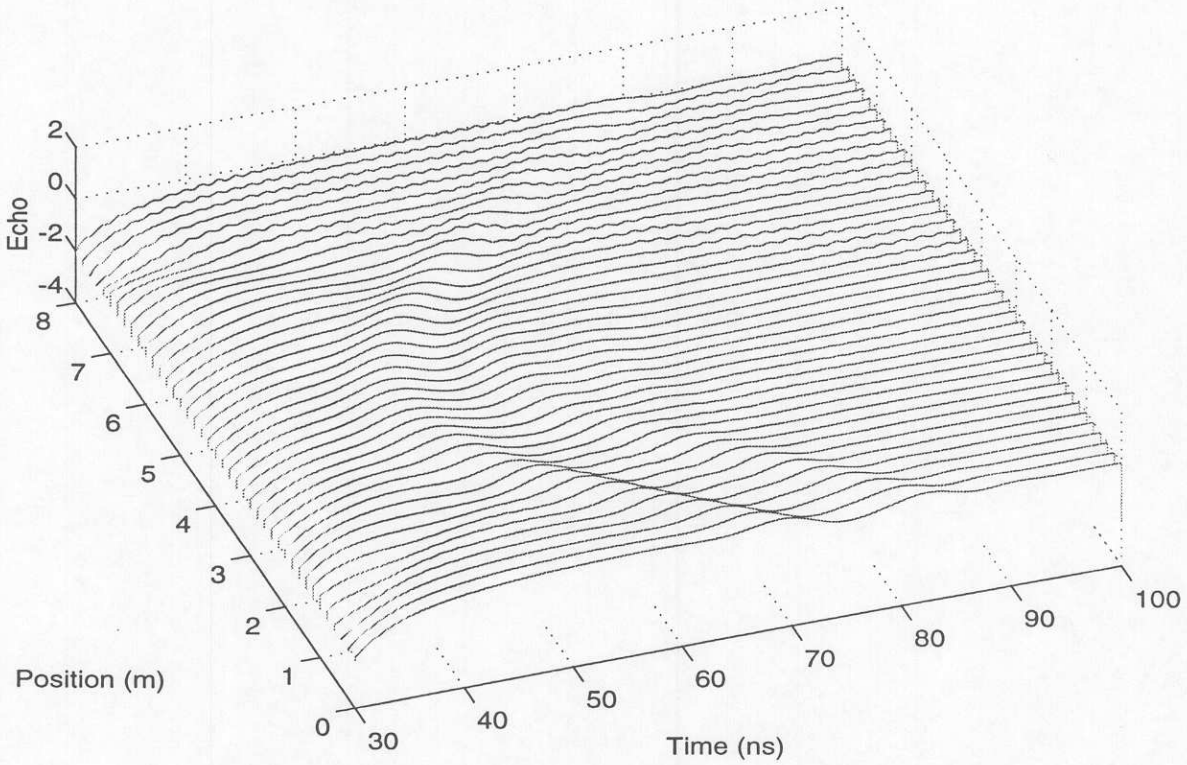

Figure 17. Simulation 1.

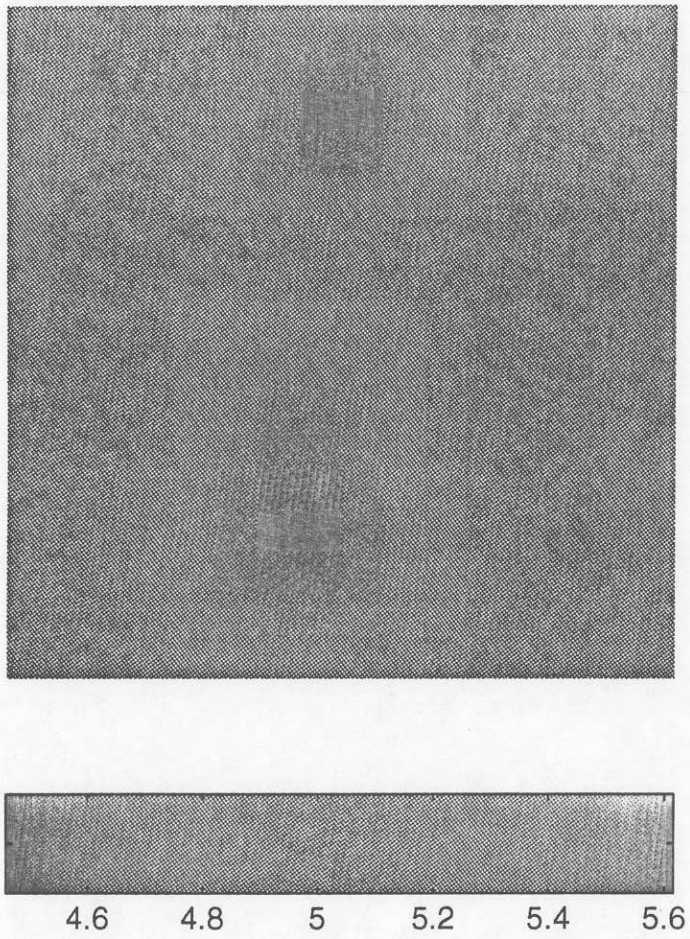

Figure 18: Simulation 2.

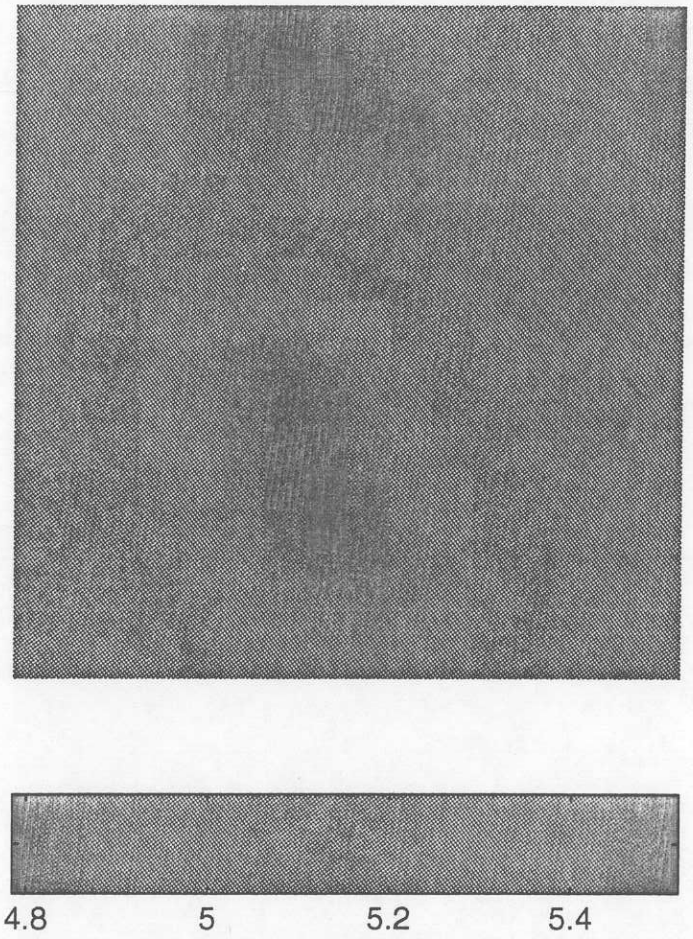

Figure 19: Simulation 3.

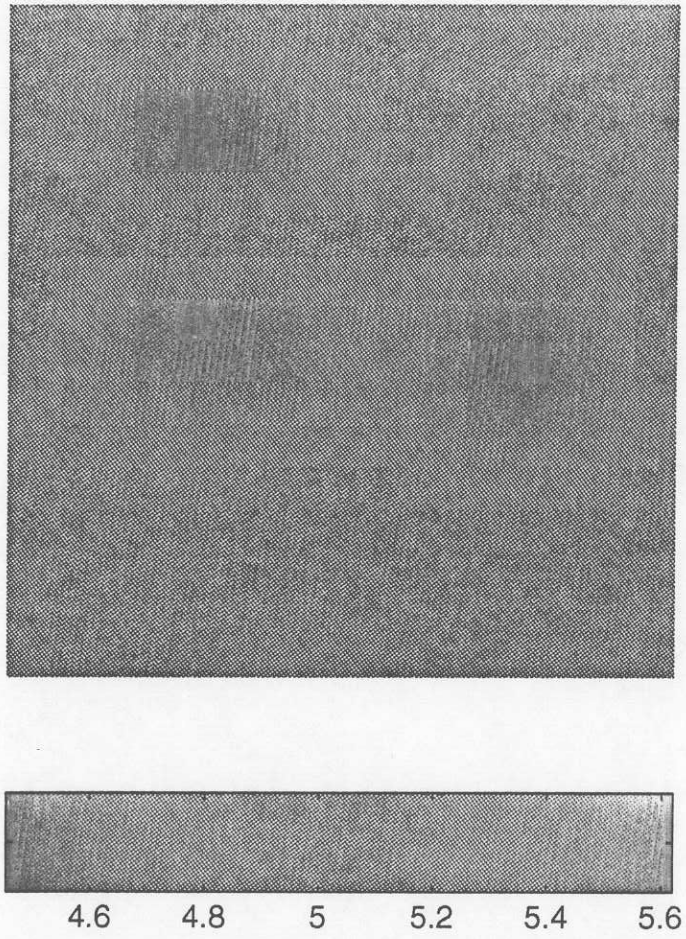

Figure 20: Simulation 4.

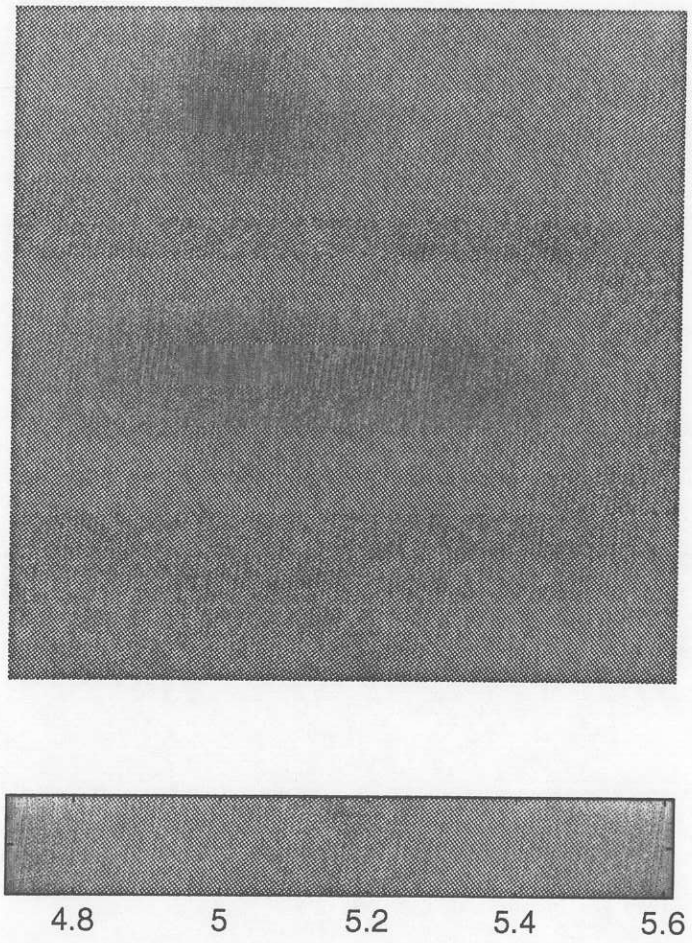

Figure 21: Simulation 5.

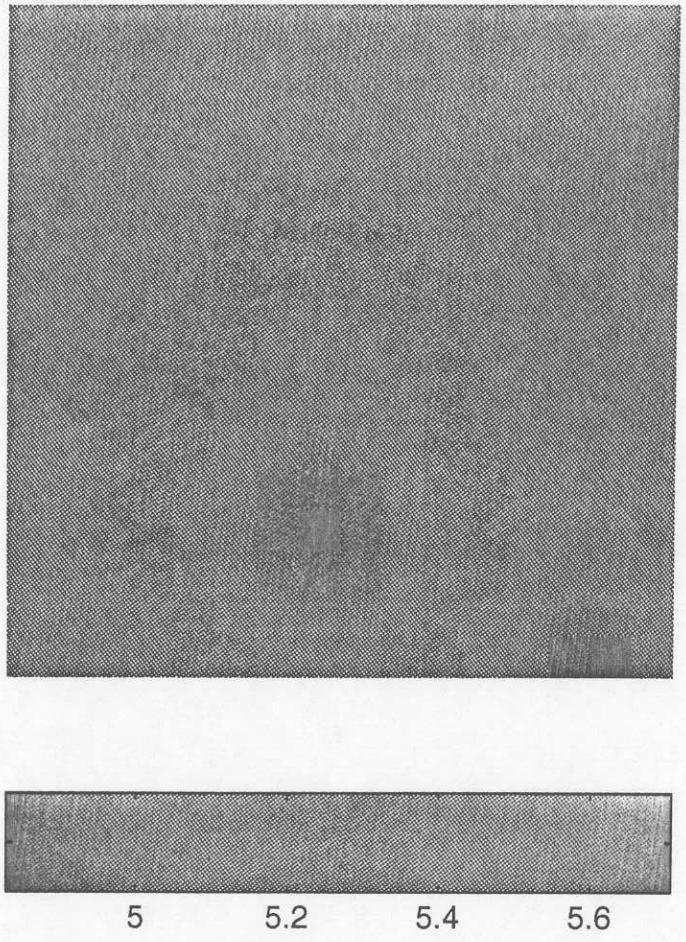

Figure 22: Simulation 6.

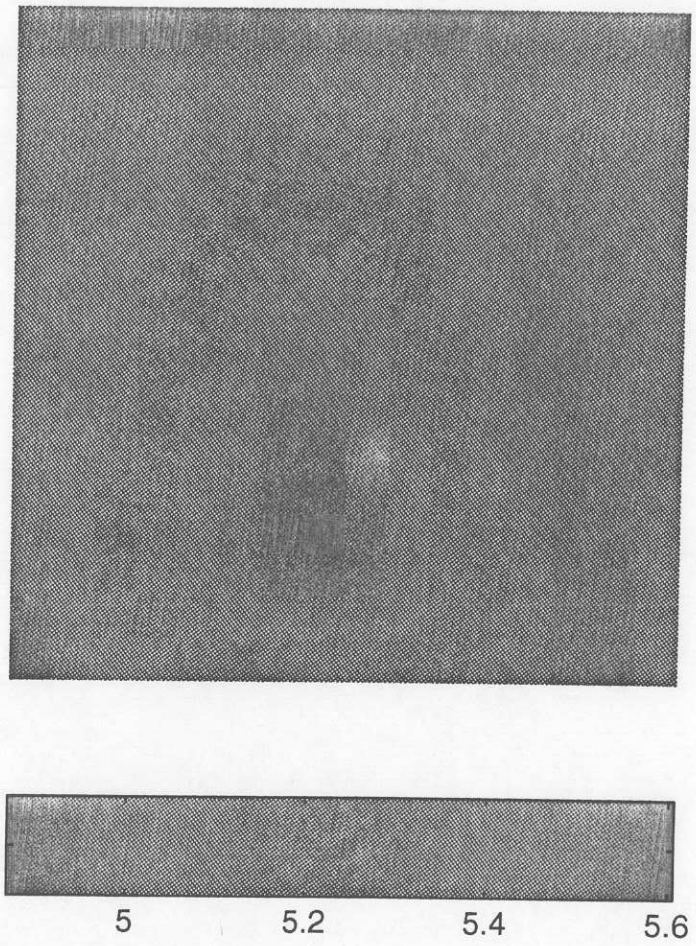

Figure 23: Simulation 7.

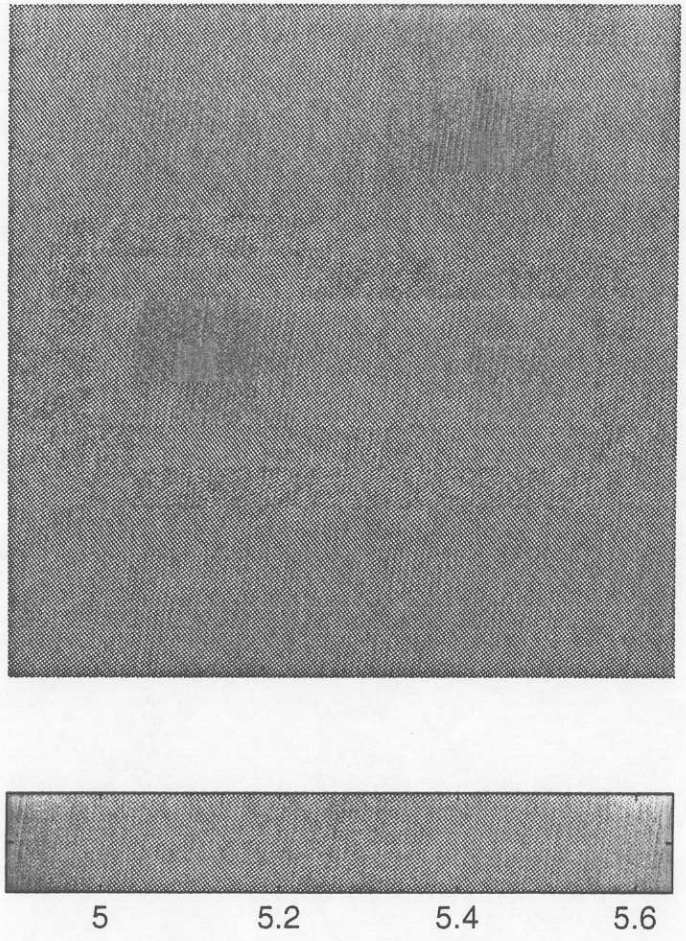

Figure 24: Simulation 8.

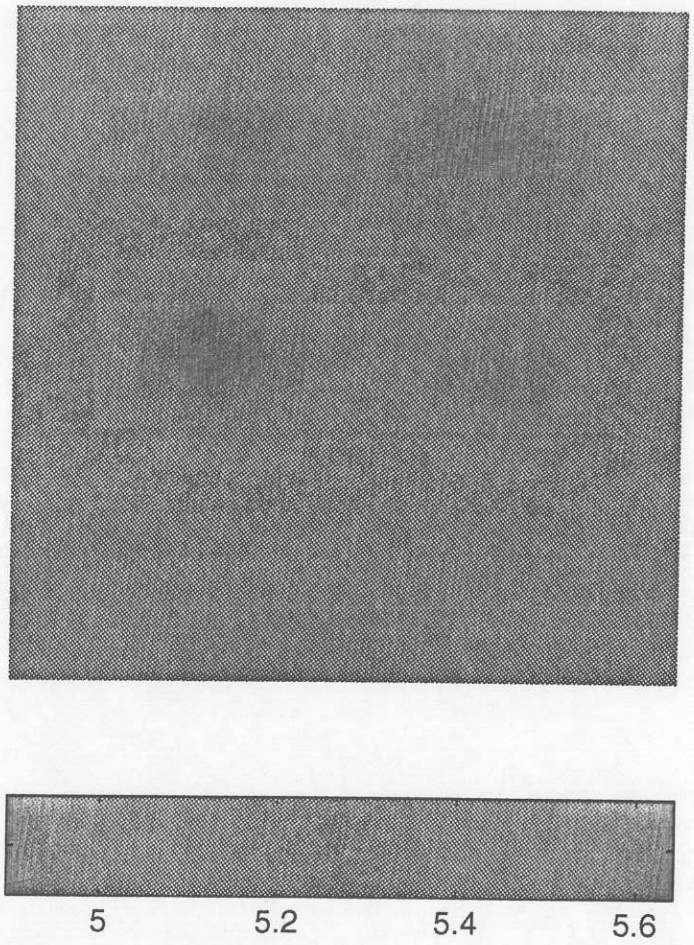

Figure 25: Simulation 9.

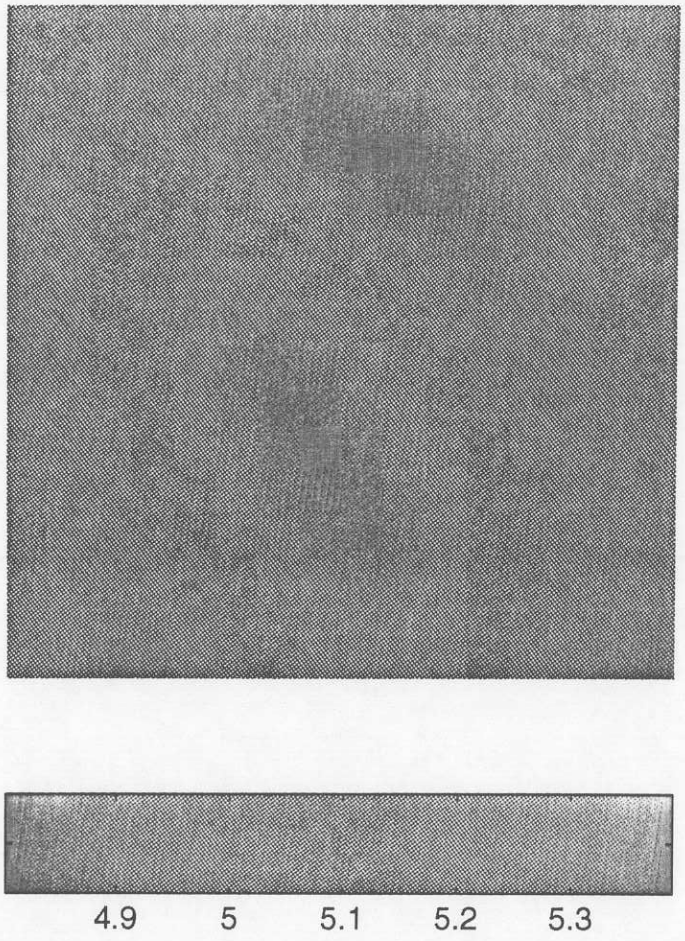

Figure 26: Simulation 10.

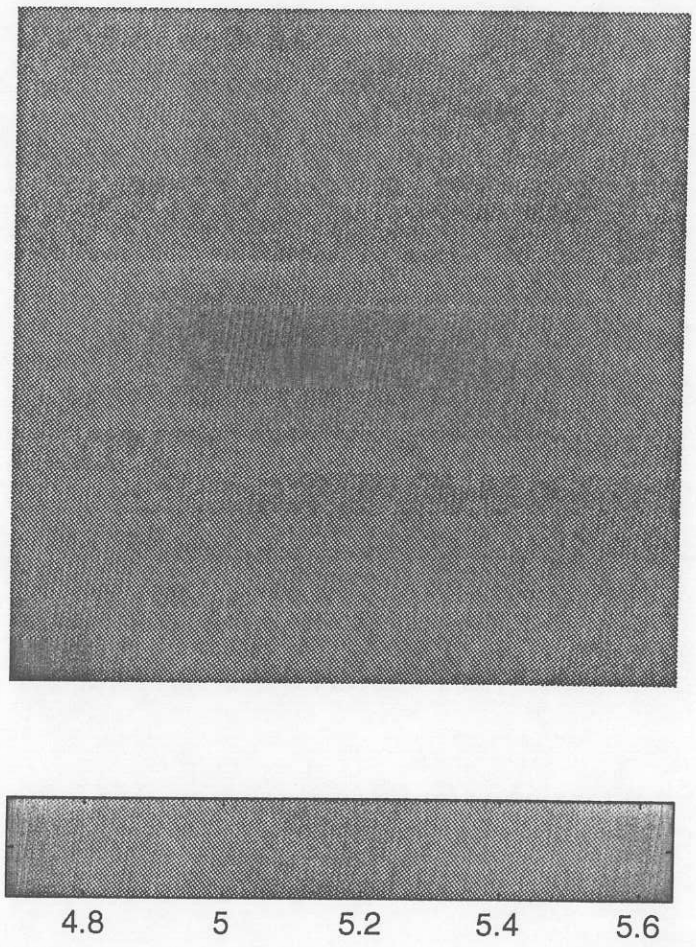

Figure 27: Simulation 11.

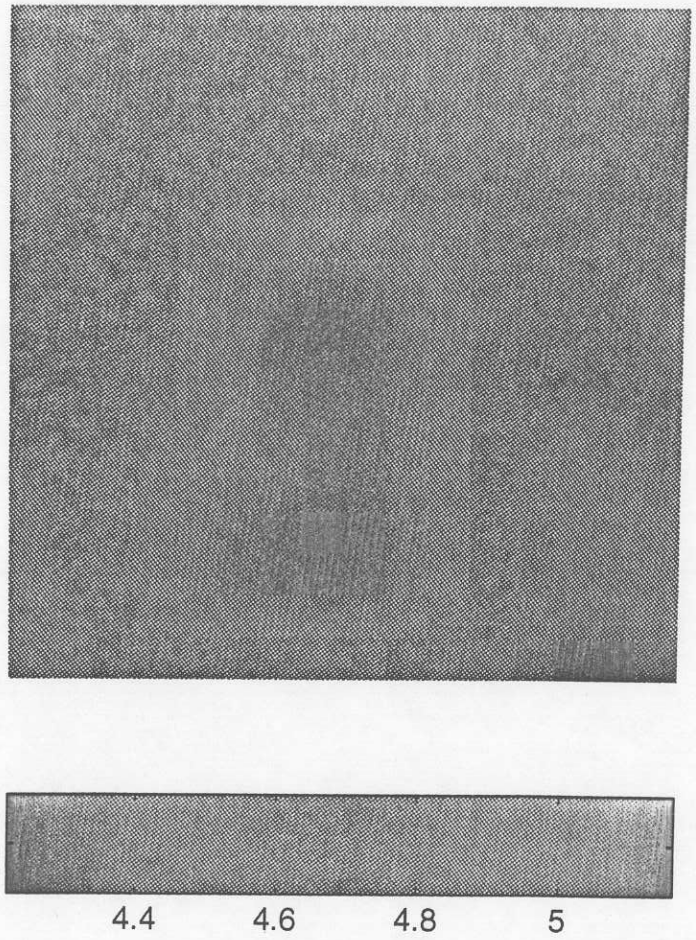

Figure 28: Simulation 12.

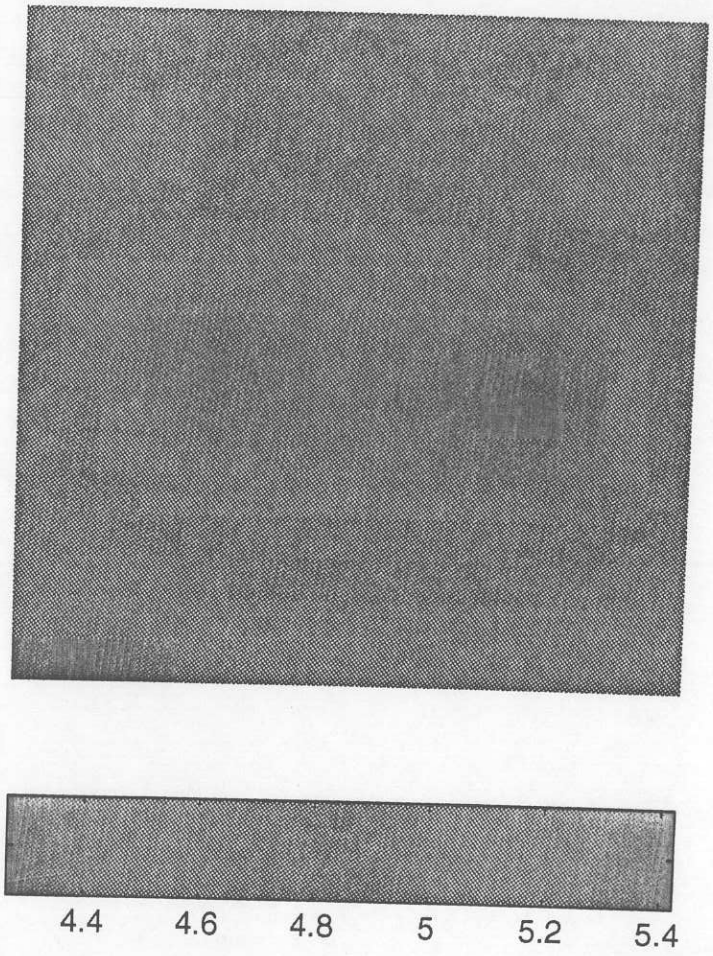

Figure 29: Simulation 13.

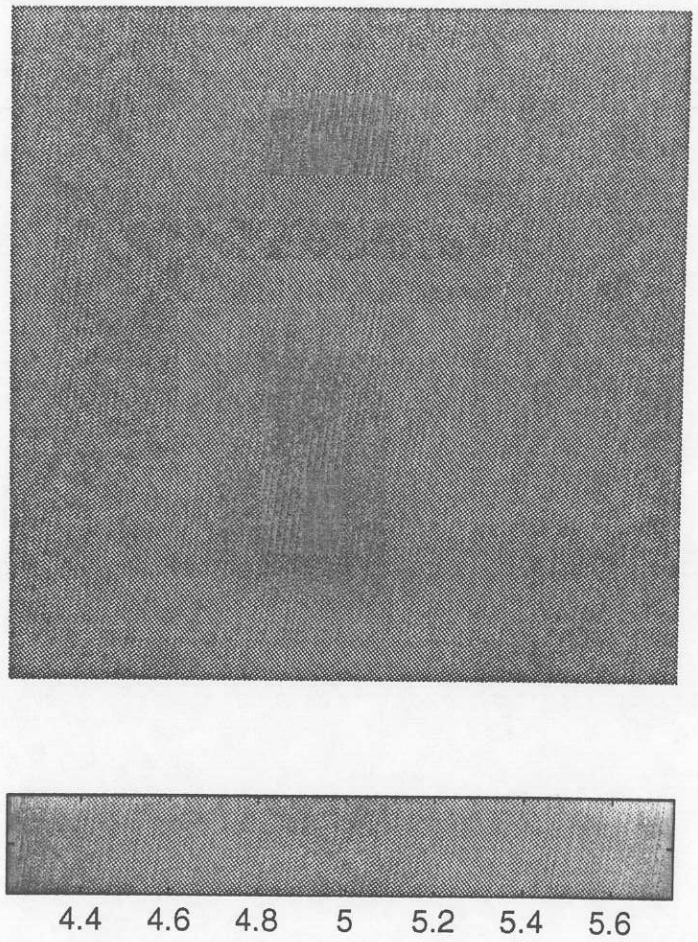

Figure 30: Simulation 14.

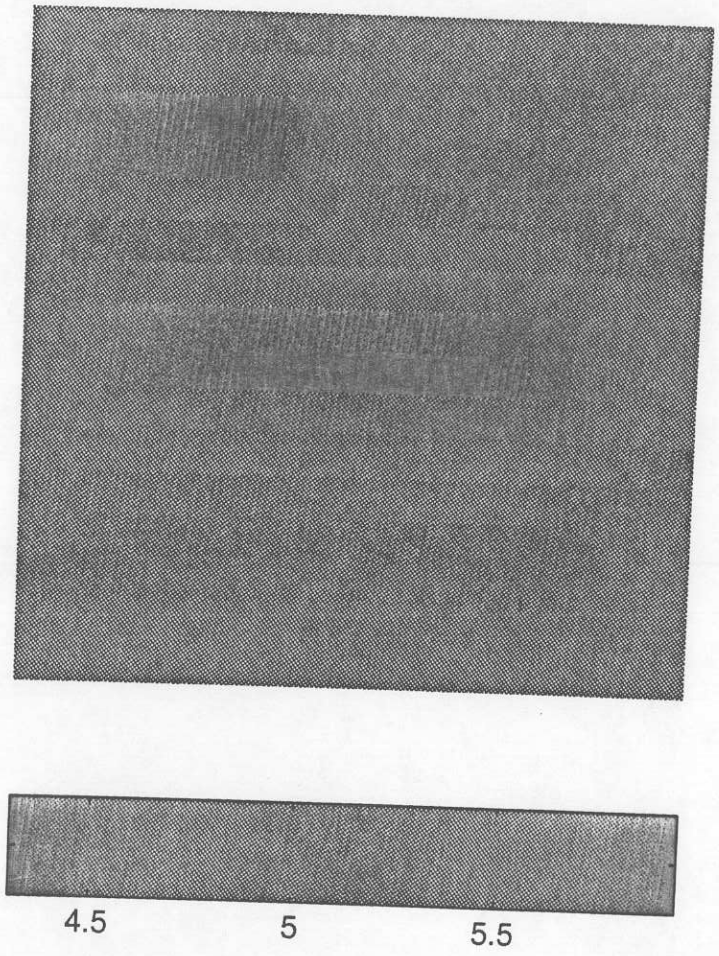

Figure 31: Simulation 15.

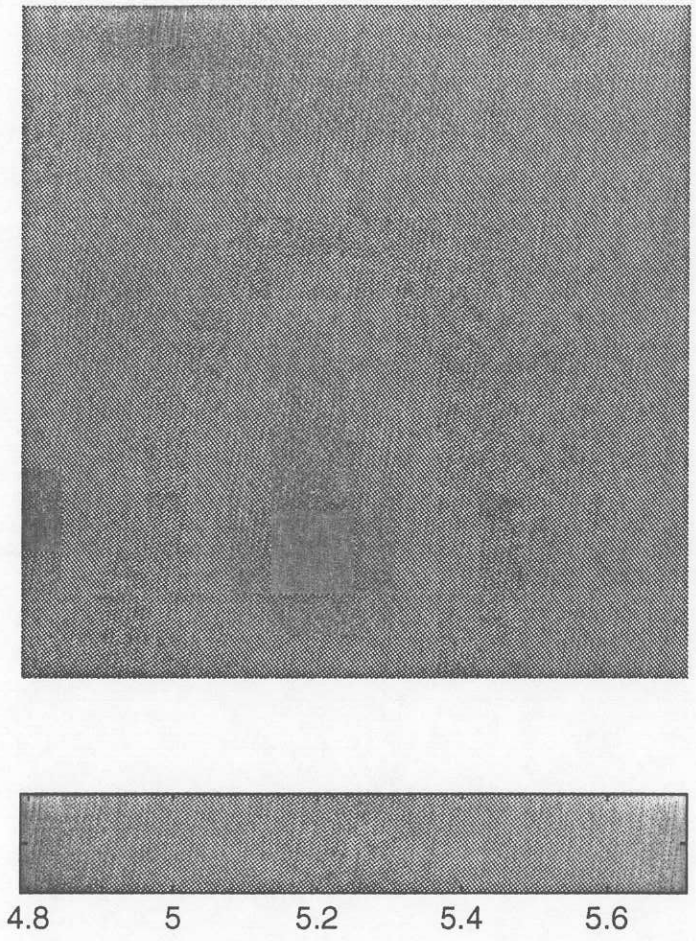

Figure 32: Simulation 16.

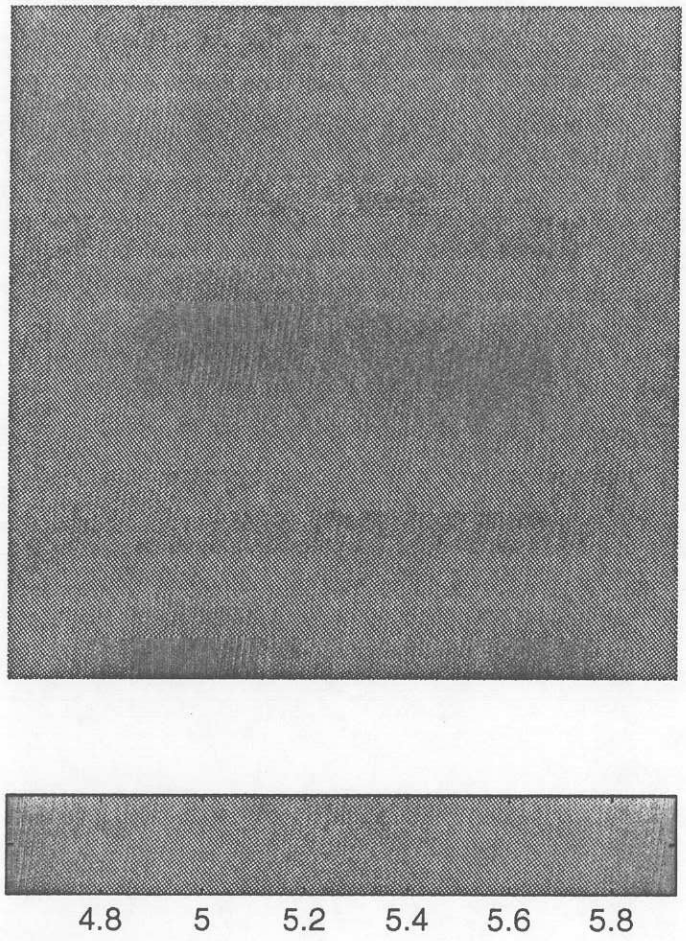

Figure 33: Simulation 17.

D. TARGET CLASSIFICATION

We have shown in the previous sections how a buried object's shape and dielectric properties can be recovered by solving an inverse electromagnetic problem. Often, the shape of the reconstructed image is a distorted version of the target's actual configuration. There are a number of reasons for such distortions: the effect of noise on measured data, deviation from the assumed background Green's function, the number of independent measurements, and the wavelength of the incident radar signal, to name a few. For images that contain multiple targets of similar size and shape, these distortion effects could easily confuse a person's ability to determine what is in the image. To overcome this problem, we investigated the use of an automated classifier to identify, or classify, objects located in the subsurface images. In the following sections we outline the work we performed on object classification using artificial neural networks and compare its performance to a traditional Bayes classifier.

Artificial network networks (ANN) have been used extensively in the remote sensing community over the last several years for pattern and object classification as well as radar data inversion [23-25]. A neural network consists of massively parallel interconnected neurons with a non-linear activation function. ANNs can be trained to form complex decisions regarding the classification of objects from distorted or noisy data [25]. These networks do not require *a-priori* information about the distribution of the input data. In this investigation, we found that a properly trained ANN can provide high classification success rates, even in the presence of much noise.

A number of steps are required before an ANN can be used to classify subsurface objects. First, the network must be trained using a number of examples or training patterns from each class that comprise a data base. Each object or pattern is referred to as a member of a class. Training of an ANN is performed with the feature vectors for which the desired outputs of the network are already known. Each feature vector consists of the samples of the spectrum obtained from the image of a subsurface target. The weights of all the connections inside the network are initialized to random values and are iteratively corrected according to the error between the computed output and the desired output at each step. The back propagation algorithm [23] is commonly used in adjusting the weights. In this technique, the error at the output is propagated backward toward the input layer to adjust the weights.

The training data for classification problems consist of either the measured data or some derived information about the target. In remote sensing the measured data are usually the total electromagnetic field measured at discrete points around the target over a particular frequency band, while the derived data could consist of a reconstructed image of the object or its spectral information. For example, one test pattern might be a thin contamination film located on top of the water table, while a second test pattern might be a chemical plume dispersing downward. The network should be trained for all possible contamination profiles that might be encountered. Once training is finished and actual data are presented to the neural network, the network produces an output vector. The unknown pattern is then classified by finding the best fit between the unknown pattern's output vector and the output vectors of the test patterns in the data base. A key to a robust classifier is to have as large a data base as possible.

The conventional Bayes classifier has been used successfully over the past few decades in pattern classification problems [26]. In this scheme, the classifier is first trained with a set of feature vectors representing several examples from different classes. During the training process, a test-vector is applied at the input of the classifier, and the classifier computes a weighted distance between the test-vector and the mean value of the training vectors from all classes. The Bayes classifier then identifies the test-vector as a member from the class for which the weighted distance attains a minimum value. The major drawback of this scheme is that it requires *a-priori* knowledge about the distribution of the input data. In most practical cases, it is difficult to acquire an exact knowledge about the probability distribution function of the input data, especially when a limited amount of data is available from each class.

In this section the basic steps of image classification are discussed. We introduce two types of neural networks, a feed-forward neural network and a probabilistic neural network, and compare their performance in subsurface target classification with a traditional Bayes classifier.

a. Major Steps for Target Classification

In this investigation, two different types of subsurface targets from the pervious section are considered for classification purposes. For Target A, Simulation 2, 3, and 10 (as shown in Table 2) are used and for Target B, Simulation 4, 5 and 11 are used. These six

images or patterns are used to train a classifier so that the classifier can recognize noisy versions of the patterns corresponding to Target A or Target B with a very high success rate. The entire pattern recognition or classification process can be divided into three major steps[26]:

1. Feature extraction from different classes of subsurface images.

2. Training a classifier using the feature vectors.

3. Testing the performance of the classifier using the feature vectors that are not used during the training process.

These three steps are discussed in detail in the following sections.

b. Feature Extraction

In the examples shown in previous section, reconstructed images of each subsurface object consisted of 16x16 pixels. The mean intensity value of each image is subtracted from the individual pixel-intensity values, and a new 16x16 pixel-intensity distribution is obtained for that image. Since the two-dimensional spectrum of an image is useful in many image classification problems, a feature vector is constructed using the samples of the spectrum of a subsurface image. The feature vectors of different classes are used to train a classifier.

A spectrum is estimated by computing the magnitude of the two-dimensional discrete Fourier transform (2D DFT) of the pixel-intensity distribution of each image. Out of the 256 (16x16) elements of the two-dimensional spectrum, only 119 samples are selected to construct a feature vector (see Figure 34). Using this procedure three different feature vectors are extracted for each type of subsurface target, corresponding to three different backgrounds. These feature vectors are then used to train a classifier. In the next section we describe a neural network classifier that is successfully used to classify subsurface targets in a noisy environment.

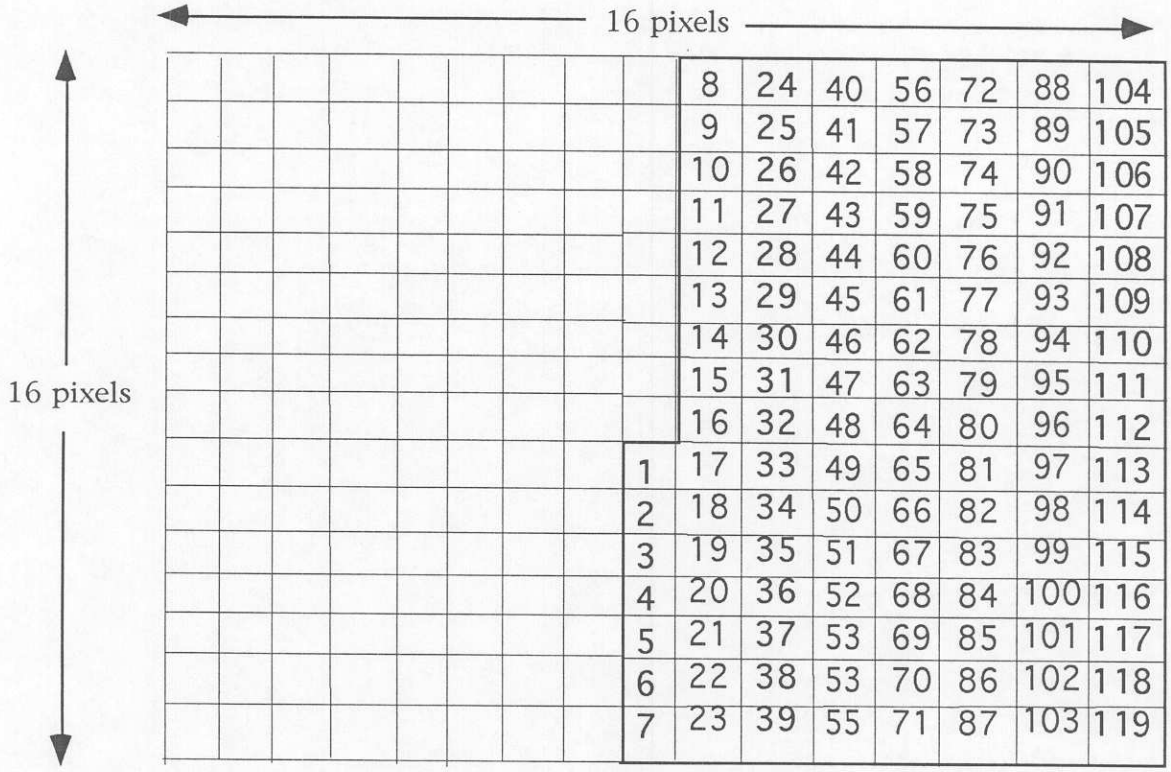

Figure 34. Construction of a feature vector using 119 samples of the 2D spectrum.

c. A Neural Network Classifier

In recent years feed-forward artificial neural networks (FANNs) [23] have been used successfully in system classification problems [24, 25]. Often, a FANN is found to provide higher successful classification rates than that achievable by a conventional statistical classifier. This superior performance of a FANN has been attributed to the fact that the FANN learns from the data itself, as is believed to be done by a human being. A FANN is also found capable of forming complex non-linear decision boundaries in the feature space, enabling correct classification of the unknown patterns even in a noisy environment. In this investigation, a FANN is trained to classify two different classes of targets from their feature vectors.

A FANN can be trained to learn about the decision boundaries in the feature space. For a FANN, learning involves iterative adjustments of the synaptic weights so that the network can map the input pattern to the desired output pattern. In this investigation, a

FANN is trained using a back-propagation learning algorithm [23]. The architecture of the FANN that is used in this investigation is shown in Figure 35 a .

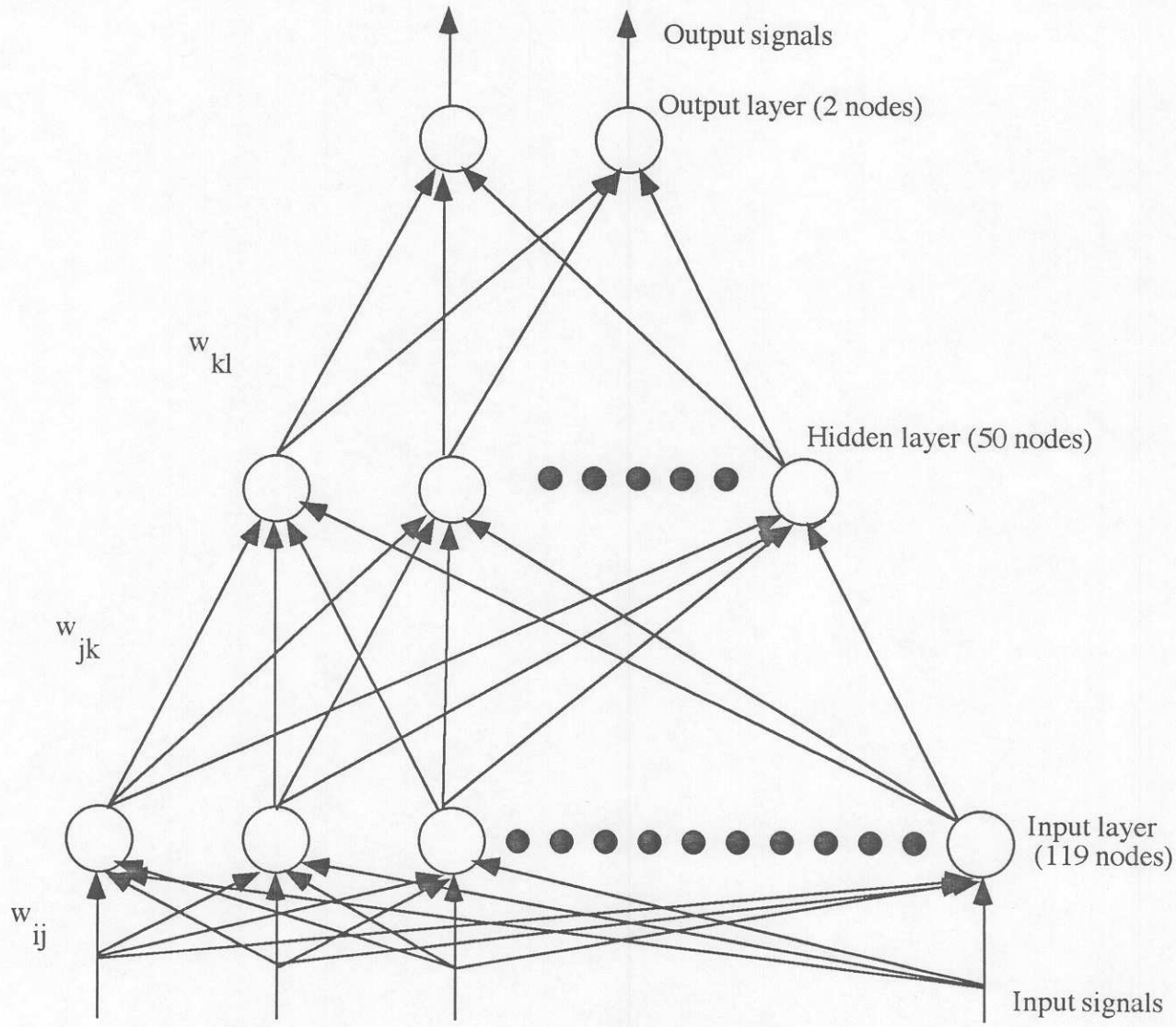

Figure 35a. Architecture of a feed-forward artificial neural network.

The FANN consists of layers of interconnecting nodes, where each node or neuron in a given layer sums up all the signal values applied at the input of the neuron and produces an output value governed by a nonlinear sigmoid function (see Figure 35 b). This output is fed to the nodes in the upper layer, after being multiplied by the synaptic weights w_{ij}. The total input to a given node i is given by [23]

$$net_i = \sum_j w_{ij} O_j + b_i, \tag{29}$$

where w_{ij} is the weight connected between the node i of one layer and node j of the adjacent lower layer; b_i is a bias weight at unit i, and O_j represents the output from node j of the lower layer. The output from node i is obtained as [23, 24]

$$O_j = \frac{1.0}{1 + e^{-net_i}}. \tag{30}$$

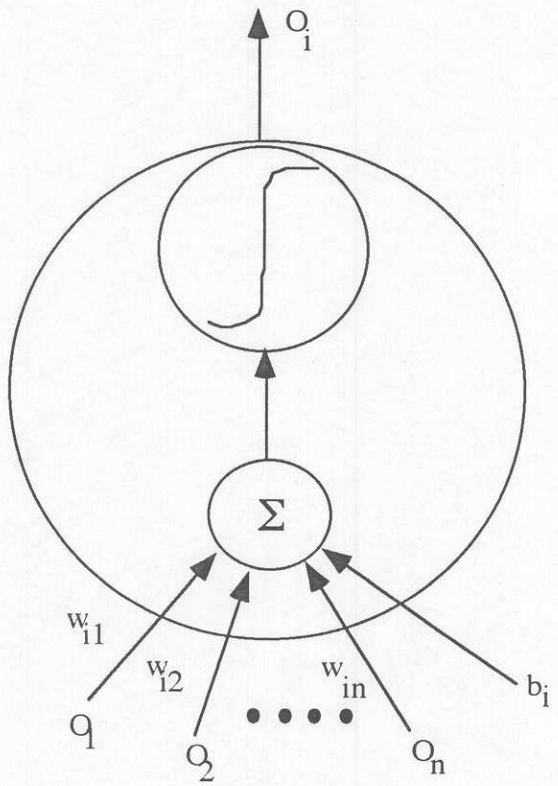

Figure 35 b. Input and output configuration of a neuron.

In the feed-forward architecture, the output from the nodes of the input layer is fed to nodes in the hidden layer, and the output from the hidden layer are fed to nodes in the output layer. Thus, the outputs from the nodes in output layer can be computed for all input patterns using (29) and (30), repeatedly. This FANN can then be trained with examples from different classes to classify unknown patterns.

d. Training a FANN

In this investigation, a FANN is trained using a back-propagation learning algorithm[23]. The training set consists of three examples each for Targets A and B. We assumed that the feature vectors corresponding to Target A belong to class 1 and those corresponding to Target B belong to class 2. The step-by-step procedure of training the network is summarized below:

1) Select a feature vector that is a member of the i^{th} class and apply it at the input of the network. Set the target or desired output value from the i^{th} node of the output layer to "1" and that from all the nodes in the output layer to "0." Compute the output values from the nodes in the output layer in the feed-forward manner [23] and calculate the error term associated with the i^{th} node in the output layer as:

$$\delta_i = O_i(1 - O_i)(t_{pi} - O_i), \tag{31}$$

where t_{pi} represents the target output value for node "i" in the output layer. Calculate the error term associated with the nodes not in the output layer as

$$\delta_i = O_i(1 - O_i)\sum_k \delta_k w_{ki}. \tag{32}$$

2) Adjust the synaptic weights as

$$\Delta w_{ij}(n) = \eta\delta_i O_j + \alpha\Delta w_{ij}(n-1), \tag{33}$$

where the indexes represent the iteration number. The constants η and α represent the learning rate and the momentum term, respectively.

3) Repeat steps 1) and 2) using a member from all classes.

4) Repeat steps 1) to 3) using all feature vectors from all classes.

5) Repeat steps 1) to 4) cyclically until the network converges. The condition for convergence is that the actual output values should be within 0.1 of the desired values for all feature vectors used during the training process.

e. Test Results

The testing process is summarized in the block diagram shown in Figure 36. Initially, a "crisp" logic-based decision-making algorithm is used to classify the input test patterns. According to this scheme, a noisy feature vector from the i^{th} class is applied at the input of the network, and the output from the output nodes of the network are computed in feed-forward manner [23]. A successful classification occurs if the output from the i^{th} node of the output layer belongs to the state "high" (or > 0.9) and all other outputs from the output layer belong to the state "low" (or < 0.1). A misclassification occurs only if the k^{th} node from the

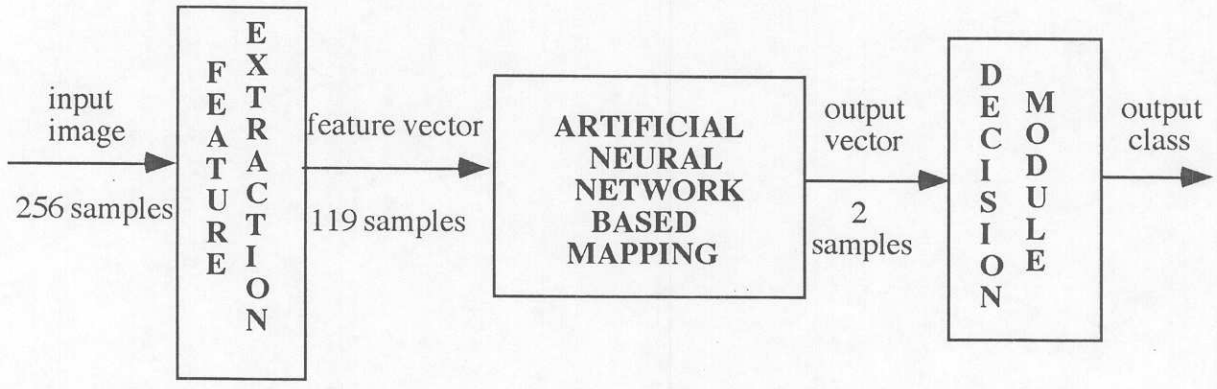

Figure 36. Block diagram of the ANN-based classification scheme.

output layer reaches the state "high" when the input feature vector belongs to the class "i." All other output configurations result in an unsuccessful classification. Using the set of optimal weights that are obtained after training the FANN and the previously mentioned crisp classification scheme, the performance of the network is tested as a function of the SNR of the subsurface image. During testing, 50 different noisy images are generated for each SNR by adding white Gaussian noise sequences to each unperturbed image. Thus, 50 different noisy feature vectors are made available for each unperturbed image at SNRs from 40 dB to 0 dB, in steps of 0 dB. The result of the testing process is shown in the Figure 37.

We also trained and tested a Bayes classifier with the same feature vectors used by the FANN, and the result is presented in Figure 37. It can be seen that the FANN provided a higher success rate than the Bayes classifier for SNRs less than or equal to 10 dB. The apparent success of the FANN is often attributed to the fact that a neural network learns from the data itself and, thus, does not require *a priori* knowledge of the probability density function of the input data. The Bayes classifier, however, assumes a Gaussian distribution of the input data.

In order to improve the success rate achieved by the FANN, a decision about the input pattern class is made using a minimum distance criteria. According to this scheme the target output vectors from the two classes are considered as $\mathbf{t_1}=(0,1)$ and $\mathbf{t_2}=(1,0)$, respectively. During the testing process, the actual outputs from the nodes in the output layer are used to construct an output vector $\mathbf{O}=(o_1,o_2)$. The input feature vector is classified as a member of class 1 if the Euclidean distance between the vectors $\mathbf{O}$ and $\mathbf{t_1}$ is smaller than that between $\mathbf{O}$ and $\mathbf{t_2}$. Otherwise, the input pattern will be classified as a member of class 2. The success rate obtained by this method is also plotted in Figure 37. It can be seen that the minimum distance classification scheme provided nearly a 100% success rate over the 40- to 0-dB range. This is a significant improvement over the performances achieved by the Bayes or FANN with a crisp logic-based classification scheme. These results clearly indicate that the neural network has the potential for finding applications as a subsurface target classifier.

Even though a FANN provides an impressive success rate in classifying subsurface targets, it often takes considerable amount of CPU time during the training process. Sometimes a FANN gets stuck in a local minimum and the network fails to converge to an acceptable solution. To overcome this problem, a Probabilistic Neural Network (PNN) has been proposed[27]. The PNN basically uses half of a complete iteration to learn about the

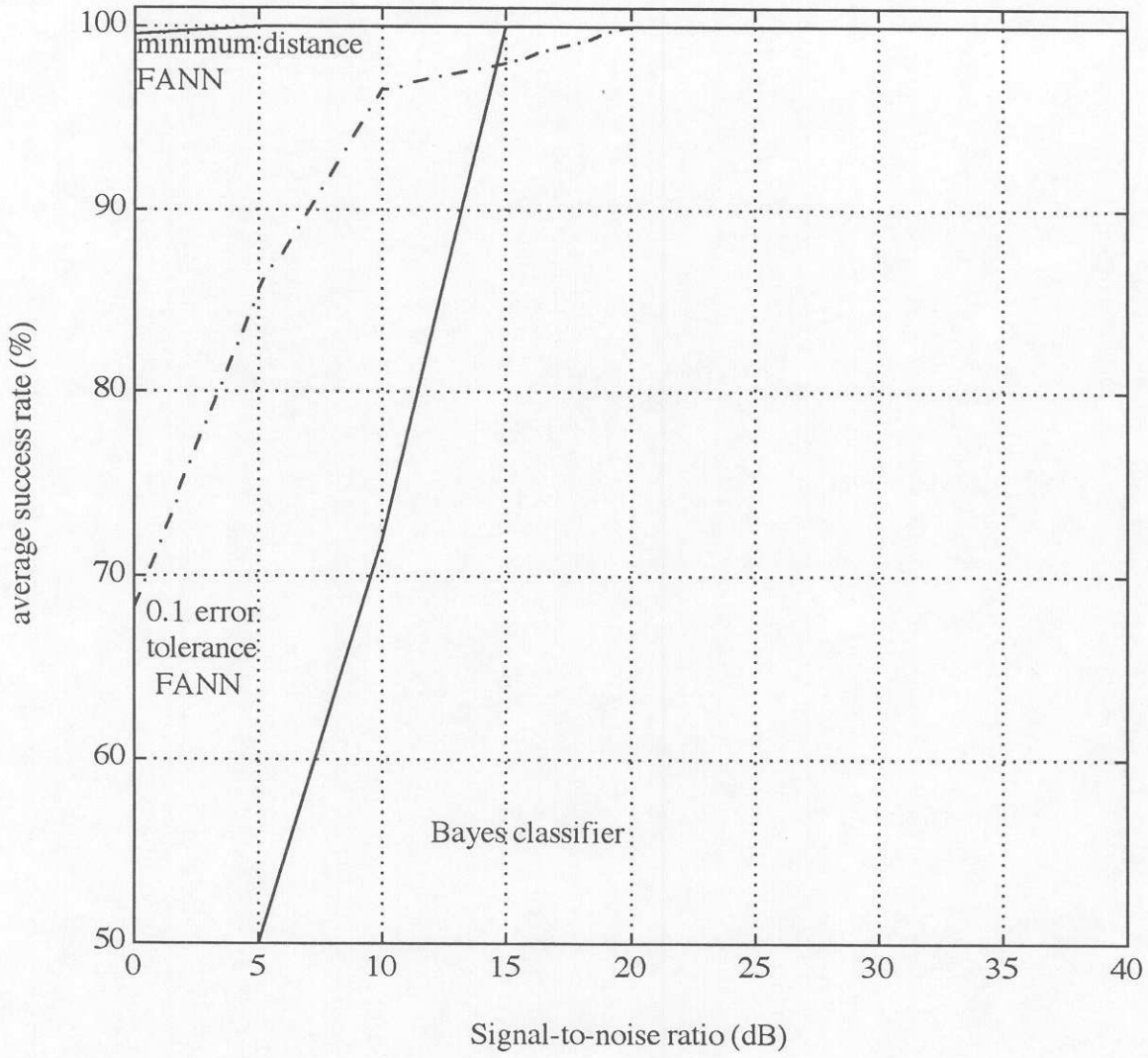

Figure 37. Success rate (%) vs. SNR for the Bayes classifier and FANN.

decision boundaries in the feature space. In the next section a PNN is introduced and its performance is compared with that of the FANN.

f. A Probabilistic Neural Network Classifier

In recent years a Probabilistic Neural Network (PNN) has been found to be useful in solving real-world pattern recognition problems. A PNN is designed to function on the basis of the estimation of the probability density functions (PDFs) for various classes as learned from the training samples [27]. It has been shown that the PNN learns about the PDFs of different classes from the sampled data almost instantaneously and uses the PDFs to compute non-linear decision boundaries between its classes.

The architecture of a PNN consists of neurons distributed over the three layers as shown in Figure 38. The input layer consists of N neurons where N is the fixed dimension of the feature vectors used for training or testing the network. The nodes in the input layer are often used to normalize the input feature vector $\mathbf{X}$ such that $\|\mathbf{X}\|=1$. The normalized vector $\mathbf{X}$ consists of elements x^k where k varies from 1 to N. The output vector from the input layer is fed to all the nodes in the hidden layer after being multiplied by the synaptic weight vectors $\mathbf{W}_{ij}$. The index "i" represents the class number, and the index "j" represents the example number of that class. The elements ($w_{ij}{}^k$) of a weight vector $\mathbf{W}_{ij}$ actually represent the elements of a feature vector from the class "i" of the j^{th} example, which is available during the training process. Thus, during training, if "q" examples are available from each of the "p" classes, the total number of nodes to be used in the hidden layer is r=pxq. From Figure 38, the total input to a node in the hidden layer is given by

$$\mathbf{X}.\mathbf{W}_{ij} = \sum_{k=1}^{N} x^k w_{ij}{}^k. \qquad (34)$$

The input-output relationship of each node in the hidden layer is governed by [29]

$$O_s = \exp(\mathbf{X}.\mathbf{W}_{ij} - 1)/\ \sigma^2 \qquad (35)$$

where s=1,2,....r, and σ is the smoothing factor that is chosen by the user. Since both $\mathbf{X}$ and $\mathbf{W}_{ij}$ are normalized, it is expected that when a test vector from class i is applied at the input

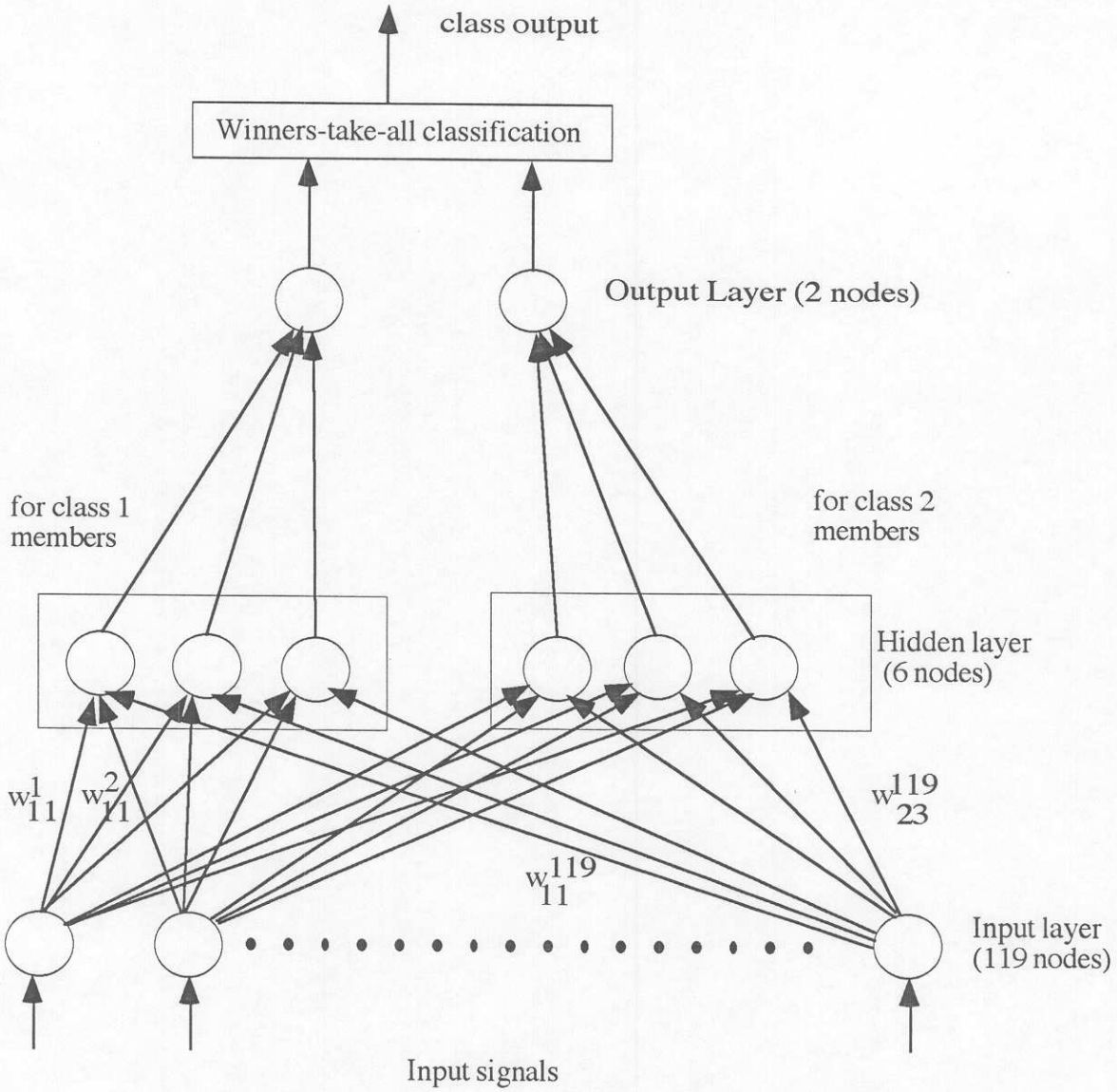

Figure 38. Architecture of a PNN.

of the PNN, the outputs from the hidden nodes that belong to the class i will have values close to unity. The outputs from the other nodes in the hidden layer will depend on the angle between the test vector $\mathbf{X}$ and the training vector $\mathbf{W}_{ij}$ in the multi-dimensional feature space. The outputs from all the nodes in the hidden layer that belong to the class i are fed to the i^{th} node of the output layer. Thus, the total number of nodes in the output layer is set to be equal to the total number of classes available (i.e., =p). Each node in the output layer sums up all the signals coming from the hidden layer and produces one output value. The test vector is

then classified as a member from the class i if the i^{th} node of the output layer provides the maximum output value.

In this investigation, three different feature vectors from each of the two classes are used to form the weight vectors W_{11}, W_{12}, W_{13}, W_{21}, W_{22}, W_{23}. The first subscript of W identifies the class and the second subscript identifies the example number of that class. Each weight vector has 119 elements, which is equal to the dimension of the feature vector. These weights are connected between the input layer and the hidden layer as shown in Figure 38. The input layer of the PNN consists of 119 nodes and the hidden layer consists of 2 (classes) x 3 (examples) =6 nodes. The output layer consists of two nodes as shown in Figure 38. The PNN is then tested with the same data set used for testing the performance of a FANN, and the success rate is presented in Figure 39.

g. Comparison of the Performance between the FANN and the PNN

It can be seen from Figure 39 that for an SNR greater than 10 dB, the PNN provided a 100% success rate. For SNR less than 10 dB, the success rate achieved by the PNN depends on the value of the smoothing parameter σ. It can be seen from Figure 39 that for σ=0.4, the success rate came very close to that achieved by a FANN. We believe that it is possible to find a value of σ for which a PNN will provide a success rate greater than or equal to that achieved by a FANN. Since the success rate achieved by a PNN depends on the choice of the smoothing factor σ, one might consider this fact as a drawback for the PNN-based classification scheme. However, it has been shown that a good value of σ can be found fairly quickly for most practical problems [27]. It has also been shown that the classification rate does not change dramatically with small changes in the value of σ. Two other limitations that are inherent in this approach are that (1) the entire training set needs to be stored for its use during the testing process, and (2) the amount of computation necessary to classify a test pattern increases with the size of the training set. However, due to the availability of cheap memory elements and fast CPUs, the PNN-based classification scheme may not impose any serious limitations.

In some areas, a PNN is found to provide major advantages over the FANN. A PNN learns from the data in real-time since it does not require supervised learning. Furthermore, a

PNN does not suffer from the local minima problem which, is a major problem for FANN when trained with the back-propagation learning algorithm.

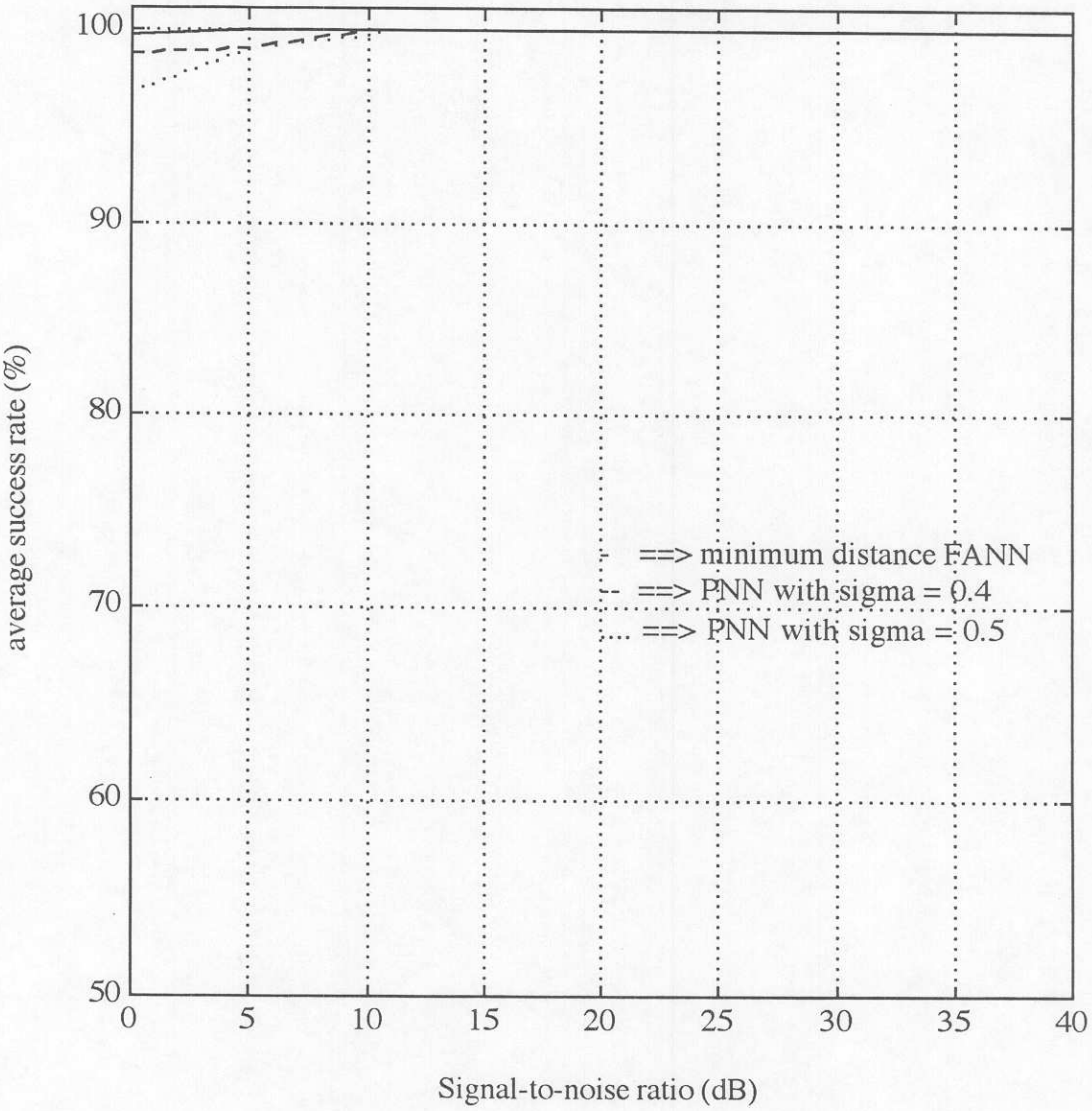

Figure 39. Success rate (%) vs. SNR for the PNN and FANN.

IV. IMPLEMENTATION

As discussed in Section II, Background Information, there are at least three ways to implement a ground-penetrating radar: impulse radar, FM-CW, or stepped FM. We propose that a stepped FM approach would be the best selection and outline our rationale in this section.

In addition to receiving a scattered field from a buried object, a radar receives other signals as well. These various signals fall into one of three categories: systemic signals, noise, and clutter. Systemic signals include the fields reflected from the air-to-soil interface and a possibly a signal directly coupled between the antennas. These undesired signals can be removed through various signal processing techniques using any of the three GPR types. Noise, another undesired signal, enters the radar through noise present in the soil, nearby electromagnetic sources (TV and radar signals for example), and noise generated in the radar itself. Techniques exist to reduce noise depending on the type of GPR used. The last type of undesired signal is clutter. Clutter is loosely defined as any signal received by the radar that is not the desired target signal or noise. Clutter will be generated by any inhomogeneities in the ground. For example, any rocks buried in the ground near the desired target will generate a scattered field and contribute to clutter.

The effects of noise, quantified in terms of signal-to-noise ratio (SNR), can be reduced depending on the type of radar and signal processing used. An impulse radar overcomes noise by transmitting high power signals. For the two types of variable frequency radars, FW-CW and stepped FM, coherent integration can be used to improve the SNR. In coherent integration, a number of individual returns are added in phase. The net effect of this process is that signal power adds, whereas the noise power, being random, remains the same. The stepped FM radar using a phase-locked frequency synthesizer offers better performance compared to an FM-CW radar.

Clutter is a much more difficult problem for GPR than is noise. In fact, clutter ultimately limits the performance of most GPRs. As mentioned above, clutter is signals received from undesired targets. Since the desired targets and clutter targets are non-moving, coherent integration will not improve the signal-to-clutter ratio (SCR). Certain types of advanced signal processing can improve the SCR depending on the type of clutter. We did not thoroughly investigate techniques to improve the SCR in this investigation.

The imaging algorithms presented in this report use monochromic, or time-harmonic, fields. In other words, the images are generated using a single frequency. For this reason the SNR performance of the stepped FM radar will outperform the impulse radar. The amount of noise entering the impulse radar is proportional to the radar's bandwidth: the larger the bandwidth the more noise enters the system. On the other hand, the bandwidth of the stepped FM radar can be made much narrower. The combination of coherent integration and a narrower frequency band of operation provides better SNR performance in the stepped FM GPR.

A key factor in using the imaging algorithms presented here is the selection of the frequency of operation. Unfortunately, there is no optimum frequency using GPR systems. The choice of frequency depends on several factors including the background soil, the desired resolution of the system, and depth of the suspected targets. The attenuation of electromagnetic waves at a given frequency will be higher for clay soils than that for sand or silt soils. In general the amount of attenuation increases with higher frequencies. Therefore, a GPR must use lower frequencies at spill sites with clay soils. In addition, the deeper a target is buried the lower the frequency must be to overcome attenuation.

A stepped FM GPR with a large system bandwidth but a small instantaneous bandwidth could easily be built. The desired operating frequency band could be selected and optimized based upon the soil type present at the site. This is another reason for selecting the stepped FM radar over the impulse GPR.

V. RECOMMENDATIONS

If developed to their full potential, the theories and techniques presented in this report could generate accurate subsurface images of suspected spill sites. These underground maps would be an invaluable tool in determining the extent of a suspected spill site. Additional work is required, however, before the imaging algorithms could be used in the field. In this section we outline a possible course for future work in this area.

Before any field experiment is performed, a number of laboratory experiments should be undertaken. Unlike field experiments, laboratory experiments provide a means to control carefully the experiment. The soil, contaminates, and hardware can be carefully monitored. We recommend that a scale model be developed for the ground-penetrating radar, soil, and contaminates.

A scale model for studying ground-penetrating radars has recently been reported [30]. The model is one-third full size and is used with an impulse GPR having significant frequency content within the range of 150 MHz to 1.5 GHz. The unique feature of this set-up is an oil-in-water emulsion used to represent various soil types. The constituents of the emulsion are oil, saline solution, and an emulsifier. By properly selecting these ingredients, the emulsion can be made to simulate the electrical properties of any soil.

A similar approach could be developed to test the imaging algorithms presented in this report. A large tank could be constructed to hold the emulsion and radar hardware. Any number of contaminates, pipes, or storage tanks could be placed in the emulsion. In addition, clutter could be added to test the performance of the algorithms as a function of signal-to-clutter ratio.

An advantage of performing such a laboratory experiment first is that the GPR would not have to be built. Instead, a vector network analyzer could be used as the GPR. While the laboratory experiment is under way the imaging algorithms should be extended to handle three-dimensional data. No new theories need to be developed for this, instead some additional programming is all that is required.

As an additional feature in helping predict GPR returns over contaminate plumes, a small study could be undertaken to incorporate the VALOR code [31] and our GPR simulator. VALOR is a PC code for simulating two-dimensional immiscible contaminate

transport in subsurface systems. This code was recently developed by researchers at The University of Michigan and was sponsored by the Electric Power Research Institute. VALOR uses a two-dimensional finite-element technique to predict the flow of organic liquids in heterogeneous soils with horizontally aligned stratum. Our GPR simulator and imaging algorithms also work on horizontally stratified heterogeneous soils. The output of VALOR would be used to generate an electrical parameter (permittivity, permeability, and conductivity) map of the soil and contaminant flow. The merging of these two codes would be a powerful tool useful in predicting GPR returns from spill sites.

VI REFERENCES

[1] Douglas, D. G., Burns, A. A., Rino, C. L., and Maresca, Jr., J. W., "A Study to Determine the Feasibility of Using A Ground-Penetrating Radar for More Effective Remediation of Subsurface Contamination." EPA report, EPA/600/r-92/089, May 1992.

[2] Abriola, L. M., K. Rathfelder, M. Maiza, and S. Yadav, "VALOR Code Version 1.0: A PC Code for Simulating Immiscible Contaminant Transport in Subsurface Systems," EPRI TR-101018. Electric Power Research Institute, Palo Alto, CA., Sept. 1992.

[3] Yee, K. S., "Numerical Solution of Initial Bounary Value Problems Involving Maxwell's Equations in Isotropic Media," *IEEE Trans. Antennas and Propagation,* vol. AP-14, no. 3, pp. 302-307, May 1966.

[4] Umashankar, K. and A. Taflove, "A Novel Method To Analyze Electromagnetic Scaterind of Complex Objects," *IEEE Trans. Electromagnetic Compat.*, vol. 24, pp. 397-405, Nov. 1982.

[5] Tirkas, P. and K. Demarest, "Modeling of Thin Dielectric Structures Using the Finite-Difference Time-Domain Technique," *IEEE Trans. Antennas and Propagation,* vol. AP-39, no. 9, pp. 1338-1344, September 1991.

[6] Luebbers, R., and Karl Kunz, *The Finite Difference Time Domain Method for Electromagnetics*, CRC Press, 1993.

[7] Demarest, K. R., "A Finite Difference-Time Domain Technique for Modeling Narrow Apertures in Conducting Scatterers," *IEEE Transactions on Antenna and Propagation,* vol. AP-35, no. 7, p. 826, July 1987.

[8] Mur, G., "Absorbing Boundary Conditions for the Finite-Difference Approximation of the Time-Domain Electromagnetic Field Equations," *IEEE Trans. Electromagnetic Compat.,* vol. EMC-23, no. 4, pp. 377-382, November 1981

[9] Mei, K. K. and J. Fang, "Superabsorption - A Method to Improve Absorbing Boundary Contitions," *IEEE Transactions on Antenna and Propagation,* vol. AP-40, no. 9, pp. 1001-1010, September 1992.

[10] Tirkas, P. A. and K. R. Demarest, "Modeling of Thin Dielectric Structures Using the Finite-Difference Time-Domain Technique," *IEEE Transactions on Antenna and Propagation*, vol. AP-39, no. 9, pp. 1338-1344, September 1991.

[11] Michiguchi, Y., K. Hiramoto, M. Nishi, F. Tatahashi, T. Ohtaka, and M. Okada, "Development of Signal Processing Methods for Imaging Buried Pipes," *IEEE Trans. on Geoscience and Remote Sensing*, vol. GE-25, no. 1, pp. 11-15, January 1987.

[12] Iizuka, K., H. Ogura, J. L. Yen, V. K. Nguyen, and J. R. Weedmark, "A Hologram Matrix Radar," *Proceedings of the IEEE*, vol. 64, no. 10, pp. 1493-1504, October 1976.

[13] Osumi, N. and K. Ueno, "Microwave Holographic Imaging Methods with Improved Resolution," *IEEE Trans. on Antennas and Propagation*, vol. AP-32, no. 10, pp. 1018-1026, October 1984.

[14] Devaney, A. J., "Geophysical Diffraction Tomography," *IEEE Trans. on Geoscience and Remote Sensing*, vol. GE-22, no. 1, pp. 3-13, January 1984.

[15] Witten, A.J. and E. Long, "Shallow Applications of Geophysical Diffraction Tomography," *IEEE Trans. on Geoscience and Remote Sensing*, vol. GE-24, no. 5, pp. 654-662, September 1986.

[16] Staney, M., A. C. Kak, and L. E. Larsen, "Limitations of Imaging with First-Order Diffraction Tomography," *IEEE Trans. on Microwave Theory and Techniques*, vol. MTT-32, no. 8, pp. 860-874, August 1984.

[17] Chew, W. C., *Waves and Fields in Inhomogeneous Media*, Van Nostrand Reinhold, New York, 1990.

[18] Danniels, D. J., D. J. Gunton, and H. F. Scott, "Introduction to Subsurface Radar," *IEE Proceedings Part F, Communications, Radar, andSignal Processing*, vol. 135, no. 4, pp.278-320, August 1988.

[19] S. Twomey, *Introduction to the Mathematics of Inversion in Remote Sensing and Indirect Measurements*, Elsevier Scientific Publishing Company, New York, 1977.

[20] A. N. Tikhonov and V. Y. Aresenin, *Solutions of Ill-Posed Problems*., John Wiley & Sons, New York, 1977.

[21] Stark, H., J. Woods, I. Paul, and R. Hingorani, "Direct Fourier Reconstruction in Computer Tomography," *IEEE Transactions on Acoustics, Speech , and Signal Processing*, vol. ASSP-29, no. 2, pp. 237-245, April 1981.

[22] Sarkar, T. K., D. D. Weiner, and V. K. Jain, "Some Mathematical Considerations in Dealing with the Inverse Problem," *IEEE Transactions on Antennas and Propagation*, vol. AP-29, no. 2, pp. 373-379, March 1981.

[23] Duda, R. O. and P. E. Hart, "Pattern Classification and Scene Analysis", John Wiley & Sons, New York, 1993.

[24] Rumelhart, D.E., G. E. Hinton and R. J. Williams, "Learning Internal Representation by Error Propagation," *Parallel and Distributed Processing: Explorations in the Microstructure of Cognition*, Vol. 1, Foundations, MIT press, Cambridge, 1986.

[25] Hush, D. R. and B. G. Horne, "Progress in Supervised Neural Networks," I*EEE Signal Processing Magazine*, January 1993.

[26] Setiawan, E. and S. Chakrabarti, "Robust Classification of Radar Signals Using a Fault-Tolerant Feed-Forward ANN: An Emperical Study," *Proceedings of the Artificial Neural Networks in Engineering*. vol. 3, pp. 455-460, ST. Louis, MO, Nov. 1993.

[27] Specht, D. F., "Probabilistic Neural Networks," *Neural Networks*, vol. 3, pp. 109-118, 1990.

[28] Chaturvedi, P., R. G. Plumb, and K. R. Demarest, "Feasibility of Ground-Penetrating Radar for Use at MGP Sites; Second Quarterly Report," RSL Technical Report 9990-2, Radar Systems and Remote Sensing Laboratory, University of Kansas, April 1993.

[29] Chaturvedi, P., R. G. Plumb, and K. R. Demarest, "Feasibility of Ground-Penetrating Radar for Use at MGP Sites; Third Quarterly Report," RSL Technical Report 9990-3, Radar Systems and Remote Sensing Laboratory, University of Kansas, July 1993.

[30] Smith, G. S. and W. R. Scott, Jr., "A Scale Model for Studying Ground Penetrating Radars," *IEEE Trans. on Geoscience and Remote Sensing*, Vol. 27, No. 4, pp 358-363, July 1989.

[31] "VALOR Code Version 1.0: A PC Code for Simulating Immiscible Contaminant Transport in Subsurface Systems," EPRI TR-101018 Project 2879-08, September 1992.